

On structure-preserving and pointwise conservative continuous DG schemes for hyperbolic systems

Rémi Abgrall · Michael Dumbser ·
Pierre-Henri Maire · Enrico Zampa

Received: date / Accepted: date

Abstract We present a new class of structure-preserving semi-discrete continuous-discontinuous Galerkin (CG-DG) finite element schemes for linear and nonlinear hyperbolic systems of partial differential equations on unstructured simplex meshes that automatically satisfy the following properties: i) the new schemes are not only cell-wise conservative, but also locally pointwise conservative everywhere, hence they satisfy the integral form of the conservation law on *arbitrary control volumes* that do not have to coincide with the mesh at all; ii) the new methods naturally satisfy the two basic vector calculus identities $\nabla \cdot \nabla \times \mathbf{A}$ and $\nabla \times \nabla Z$ exactly pointwise locally and globally everywhere on the discrete level; iii) for linear symmetric hyperbolic systems the schemes are naturally energy conservative for the square energy, i.e. nonlinearly stable in the L^2 norm. The key ingredient of the new CG-DG schemes is the use of two different but compatible approximation spaces: the classical DG space \mathcal{U}_h^N of discontinuous piecewise polynomials of degree up to N and a classical finite element space \mathcal{W}_h^{N+1} of globally continuous piecewise polynomials of degree $N + 1$. In the new CG-DG schemes, the discrete solution \mathbf{u}_h is sought in \mathcal{U}_h^N , while a suitable *discrete flux field* $\tilde{\mathbf{f}}_h$ is computed in \mathcal{W}_h^{N+1} . For $N = 0$ our new schemes are directly related to cell-centered finite volume schemes with suitable vertex-based fluxes. All claimed properties of the schemes are first mathematically proven and are then also verified via suitable numerical tests. We show applications of our approach to three hyperbolic systems: i) the equations of linear acoustics, in which the velocity field

Rémi Abgrall
Institut für Mathematik, Universität Zürich, Wintherthurerstrasse 190, CH 8057 Zürich, Switzerland
E-mail: remi.abgrall@math.uzh.ch
Michael Dumbser
Laboratory of Applied Mathematics, University of Trento, Via Mesiano 77, 38123 Trento, Italy.
E-mail: michael.dumbser@unitn.it
Pierre-Henri Maire
CEA CESTA, 33116 Le Barp, France.
E-mail: pierre-henri.maire@cea.fr
Enrico Zampa
Faculty of Mathematics, Universität Wien, Oskar-Morgenstern-Platz 1, 1090 Vienna, Austria.
E-mail: enrico.zampa@univie.ac.at

must remain curl free if it was so at the initial time; ii) the vacuum Maxwell equations in the absence of charges, for which the magnetic and the electric field must remain divergence-free for all times if they were initially divergence-free; iii) the Euler equations of compressible gas dynamics.

Keywords continuous-discontinuous Galerkin finite element schemes; linear and nonlinear hyperbolic systems; structure-preserving schemes; discrete flux field; discrete vector calculus identities; divergence-free and curl-free schemes; applications to the equations of linear acoustics, the vacuum Maxwell equations and to the nonlinear compressible Euler equations

1 Introduction

First order hyperbolic conservation laws with stationary differential constraints (involutions) are of fundamental importance in continuum physics. Probably the most well-known involution is the divergence-free property of the magnetic field in the case of the Maxwell and magnetohydrodynamics (MHD) equations. This mathematical property of the magnetic field is equivalent to the physical statement that there exist no magnetic monopoles. Similarly, in computational solid mechanics, the inverse deformation gradient, being a gradient, must remain curl-free for all times.

The Yee scheme [101] was the first compatible discretization of the time-domain Maxwell equations and was based on a staggered mesh that allowed to define compatible discrete derivative operators so that the discrete magnetic field remains always divergence-free if it was initially divergence-free.

Since the seminal work of Yee many different numerical schemes have been designed in order to satisfy the two classical vector calculus identities exactly also at the discrete level, namely that the discrete divergence of a discrete curl must be zero and that the discrete curl of a discrete gradient must vanish. Without pretending to be complete, we refer the interested reader to the well-known family of mimetic finite difference schemes [66, 70, 79], compatible finite volume schemes [15, 16, 60] and compatible finite elements [10, 11, 28, 30, 62, 80–82, 86, 102, 103].

While the divergence-free property of the magnetic field has almost immediately attracted the interest of researchers in numerical analysis, compatible schemes that preserve the curl-free property of a vector field exactly on the discrete level have been developed much later, see e.g. [12, 19, 34, 68, 69, 88]. Very recently, notable progress in the field of exactly constraint-preserving finite volume and discontinuous Galerkin schemes has been also achieved in [17, 93] and [5, 83, 84]. Compatible discrete differential operators are also essential in the construction of staggered and cell-centered Lagrangian schemes, see e.g. [23, 31, 41, 72, 77, 78, 91] and references therein, as they allow for a natural compatibility with the so-called geometric conservation law (GCL). At first order of accuracy, the method presented in this paper is actually closely related to [20, 21, 23, 78], but on fixed meshes in Eulerian coordinates and not on moving meshes. These methods require the computation of numerical fluxes on the vertices of the mesh, which is linked to the construction of genuinely multidimensional Riemann solvers, see e.g. [8, 13, 14, 38, 40, 43, 55, 56] and its gen-

eralization to arbitrary co-dimension of the mesh via the composite finite volume approach introduced in [18, 24, 63].

The key ingredient of the new CG-DG schemes introduced in this paper is the use of two different but *compatible* approximation spaces, as in [5]: first, a DG space \mathcal{U}_h^N of discontinuous piecewise polynomials of degree up to N and second, a classical finite element space \mathcal{W}_h^{N+1} of globally continuous piecewise polynomials of degree $N + 1$. In the new CG-DG schemes, the discrete solution \mathbf{u}_h is sought in \mathcal{U}_h^N , while a suitable *discrete flux field* $\tilde{\mathbf{f}}_h$ is computed in \mathcal{W}_h^{N+1} . In the 1D case our methods are closely related to the so-called flux reconstruction (FR) method [9, 33, 58, 65, 67, 98] but in the unstructured case treated in this paper, the two methods are completely different, see e.g. [33] and related spectral differences on unstructured grids [71, 100]. Since different approximation polynomials are used for the representation of the state vector and of the flux tensor, the new CG-DG approach presents also some common ingredients with $P_N P_M$ and reconstructed DG schemes, see e.g. [45, 74, 75, 99]. However, we view the new method rather as an extension and generalization of our previous work [5].

The new CG-DG schemes introduced in this paper have the following features and properties:

- (i) they rely on a *discontinuous* piecewise polynomial representation of the state vector $\mathbf{u}_h \in \mathcal{U}_h^N$ in the DG space of degree N and on a *globally continuous* representation of the discrete numerical flux field $\tilde{\mathbf{f}}_h \in \mathcal{W}_h^{N+1}$ in the continuous finite element space of degree $N + 1$;
- (ii) they are exactly pointwise conservative everywhere and also conservative on arbitrary control volumes that do not need to coincide with the mesh;
- (iii) they are provably nonlinearly stable in the L^2 norm for linear symmetric hyperbolic systems
- (iv) the discrete differential operators appearing in the method satisfy a discrete Schwarz theorem and therefore our CG-DG schemes satisfy the two classical vector calculus identities $\nabla \times \nabla Z = 0$ and $\nabla \cdot \nabla \times \mathbf{A} = 0$ exactly also on the discrete level, pointwise inside each element and also across element interfaces.

The rest of this paper is organized as follows: in Section 2 we introduce the numerical method and give more details for the special case $N = 0$ in Section 3. In Section 4 we analyze the scheme and prove its properties. In Section 5 we show a more efficient way to compute the discrete flux field compared to the L^2 projection used in Section 2. Numerical results are shown in Section 6 and the Conclusions are drawn in Section 7.

2 Numerical method

2.1 Governing PDE under consideration

We present the numerical method for the general case of a nonlinear system of hyperbolic conservation laws

$$\partial_t \mathbf{q} + \nabla \cdot \mathbf{f} = 0, \quad (1)$$

with $\mathbf{q} = \mathbf{q}(\mathbf{x}, t)$ the state vector and $\mathbf{f} = \mathbf{f}(\mathbf{q})$ the flux tensor. Furthermore, t is the time and \mathbf{x} the vector of spatial coordinates $\mathbf{x} \in \Omega \subset \mathbb{R}^d$, with Ω the computational domain and d the number of space dimensions. Throughout this paper we assume the system (1) to be hyperbolic. We will also consider the special case of linear symmetric-hyperbolic systems, in which $\mathbf{f}(\mathbf{q})$ is a linear function of \mathbf{q} and the corresponding matrices appearing in the flux are symmetric. The computational domain Ω is discretized at the aid of a set of conforming and non-overlapping simplex elements T_k and the triangulation / tetrahedrization of Ω is denoted by $\mathcal{T}_h = \bigcup T_k$. In this paper we furthermore denote by the set \mathcal{E}_h the skeleton of the mesh, i.e. the union of all edges (2D) or faces (3D) of all elements T_k .

2.2 Compatible approximation spaces

The essence of the CG-DG scheme is the use of two different approximation spaces. A classical discontinuous Galerkin finite element space \mathcal{U}_h^N of discontinuous piecewise polynomials of degree N and a classical continuous finite element space \mathcal{W}_h^{N+1} of globally continuous piecewise polynomials of degree $N + 1$. It is obvious that spatial derivatives of solutions in the continuous FEM space \mathcal{W}_h^{N+1} can be *exactly* represented in the DG space \mathcal{U}_h^N . This is indeed a fundamental key property of the particular choice of \mathcal{U}_h^N and \mathcal{W}_h^{N+1} .

We now make the following ansatz for the discrete solutions of (1): The vector $\mathbf{q} = \mathbf{q}(\mathbf{x}, t)$ will be approximated in \mathcal{U}_h^N by a DG scheme

$$\mathbf{u}_h(x, t) = \sum_j \phi_j(\mathbf{x}) \hat{\mathbf{u}}_j(t) := \phi_j(\mathbf{x}) \hat{\mathbf{u}}_j(t) \in \mathcal{U}_h^N, \quad (2)$$

with spatial basis functions $\phi_j(\mathbf{x}) \in \mathcal{U}_h^N$ and time-dependent degrees of freedom $\hat{\mathbf{u}}_j(t)$. Since \mathbf{u}_h is *discontinuous*, the particular choice of the DG basis functions is not crucial. Here we simply use classical nodal Lagrange basis functions of degree N within each element. Throughout this paper we will make use of the Einstein summation convention which implies summation over two repeated indices. The \mathbf{u}_h are allowed to *jump* from one element T_k to another. We then introduce the following auxiliary discrete solution represented in the continuous FEM space:

$$\tilde{\mathbf{w}}_h(x, t) = \sum_j \psi_j(\mathbf{x}) \hat{\mathbf{w}}_j(t) := \psi_j(\mathbf{x}) \hat{\mathbf{w}}_j(t) \in \mathcal{W}_h^{N+1}, \quad (3)$$

with spatial basis functions $\psi_j(\mathbf{x}) \in \mathcal{W}_h^{N+1}$ and time-dependent degrees of freedom $\hat{\mathbf{w}}_j(t)$. Since $\tilde{\mathbf{w}}_h$ is *globally continuous* the natural choice for the basis functions is the classical Lagrange basis of continuous finite elements of degree $M = N + 1$. The auxiliary solution $\tilde{\mathbf{w}}_h$ can be readily obtained from the DG solution \mathbf{u}_h via a suitable projector $\mathbf{\Pi}_h$ from \mathcal{U}_h^N in \mathcal{W}_h^{N+1} as

$$\tilde{\mathbf{w}}_h = \mathbf{\Pi}_h \mathbf{u}_h. \quad (4)$$

One may choose, for example, L^2 projection as a natural projector $\mathbf{\Pi}_h$, i.e. by requiring

$$\int_{\Omega} \psi_i(\mathbf{x}) \tilde{\mathbf{w}}_h(\mathbf{x}, t) d\mathbf{x} = \int_{\Omega} \psi_i(\mathbf{x}) \mathbf{u}_h(\mathbf{x}, t) d\mathbf{x}, \quad \forall \psi_i \in \mathcal{W}_h^{N+1}. \quad (5)$$

Inserting (2) and (3) into (5) one obtains in index notation

$$\int_{\Omega} \psi_i \psi_j d\mathbf{x} \hat{\mathbf{w}}_j(t) = \int_{\Omega} \psi_i \phi_j d\mathbf{x} \hat{\mathbf{u}}_j(t), \quad (6)$$

which allows to compute the degrees of freedom of the auxiliary FEM solution $\hat{\mathbf{w}}_j$ from the degrees of freedom $\hat{\mathbf{u}}_j$ of the DG solution. Note that this operation requires the inversion of the global mass matrix of the continuous finite elements. Since the global mass matrix is symmetric and positive definite, one can use a classical matrix-free conjugate gradient method to solve the problem iteratively and efficiently, see [61]. To improve the efficiency of this procedure, see Section 5 below.

2.3 Discrete flux field

We now also introduce a discrete representation of the flux tensor, denoted throughout this paper as the *discrete flux field* and which is defined as follows:

$$\tilde{\mathbf{f}}_h(\mathbf{x}, t) = \sum_j \psi(\mathbf{x})_j \hat{\mathbf{f}}_j(t) := \psi_j(\mathbf{x}) \hat{\mathbf{f}}_j(t) \in \mathcal{W}_h^{N+1}. \quad (7)$$

Since the continuous finite element basis is a *nodal* Lagrange basis, one simply carries out a *pointwise flux evaluation* in the finite element nodes as

$$\hat{\mathbf{f}}_j(t) = \mathbf{f}(\hat{\mathbf{u}}_j(t)). \quad (8)$$

Eqns. (6) and (8) allow to compute the degrees of freedom of the discrete flux field $\tilde{\mathbf{f}}_h$ in terms of the degrees of freedom of the DG solution \mathbf{u}_h . In alternative, the degrees of freedom of the discrete flux field could also have been obtained via L^2 projection as follows:

$$\int_{\Omega} \psi_i(\mathbf{x}) \tilde{\mathbf{f}}_h(\mathbf{x}, t) d\mathbf{x} = \int_{\Omega} \psi_i(\mathbf{x}) \mathbf{f}(\tilde{\mathbf{w}}_h(\mathbf{x}, t)) d\mathbf{x}. \quad (9)$$

However, this is a line of research that was not further followed and throughout this paper we simply use the nodal evaluation (8), i.e. *interpolation* and *not* L^2 projection of the discrete flux field.

2.4 New CG-DG scheme

We now have all ingredients to introduce the new CG-DG scheme. Multiplication of (1) with a test function $\phi_i \in \mathcal{U}_h^N$, integration over an element $T_k \in \mathcal{T}_h$ and replacing the state vector \mathbf{q} by the discrete solution \mathbf{u}_h and the flux tensor \mathbf{f} by the discrete flux field yields

$$\int_{T_k} \phi_i \partial_t \mathbf{u}_h d\mathbf{x} + \int_{T_k} \phi_i \nabla \cdot \tilde{\mathbf{f}}_h d\mathbf{x} = 0, \quad \forall \phi_i \in \mathcal{U}_h^N. \quad (10)$$

After inserting the ansatz (2) and (7) into (10) one obtains in terms of the degrees of freedom

$$\int_{T_k} \phi_i \phi_j d\mathbf{x} \frac{d\hat{\mathbf{u}}_j}{dt} + \int_{T_k} \phi_i \nabla \psi_j d\mathbf{x} \cdot \hat{\mathbf{f}}_j = 0, \quad \forall \phi_i \in \mathcal{U}_h^N. \quad (11)$$

Since the discrete flux field is *globally continuous*, no integration by parts and no further steps are needed. The new semi-discrete CG-DG scheme is completely defined by (10), making obviously use of (6), (7) and (8). As usual in RKDG schemes, time integration is performed at the aid of classical or TVD Runge-Kutta schemes of suitable order.

2.5 Compatible pair of discrete nabla operators

Based on the ideas first outlined in [5] and making use of the two compatible approximation spaces \mathcal{U}_h^N and \mathcal{W}_h^{N+1} a pair of compatible discrete nabla operators is introduced. The subscripts a and c will be used for the DG degrees of freedom in a cell (triangle / tetrahedron T_k) and the subscripts p and q for the nodal degrees of freedom of the continuous FEM. Furthermore, tensor indices of physical fields are denoted by i, j, k, l and m , respectively.

2.5.1 Discrete primary nabla operator

We define the rank three stiffness tensor as

$$\mathbb{K} = \{\mathbf{K}_{cp}\} = \int_{\Omega} \phi_c \nabla \psi_p d\mathbf{x},$$

or, equivalently, in Einstein index notation,

$$K_{cpm} = \int_{\Omega} \phi_c \partial_m \psi_p d\mathbf{x}.$$

Note that this discrete operator directly appears in the CG-DG scheme (11) above. To get the discrete primary nabla operator we multiply with the inverse of the element-local mass matrix of the DG scheme, which is easy to compute, in particular for orthogonal basis functions, see e.g. [44],

$$D_{ac} = \int_{\Omega} \phi_a \phi_c d\mathbf{x}$$

i.e.

$$\nabla_c^p = D_{ca}^{-1} \mathbf{K}_{ap}, \quad \text{or,} \quad (\partial_m)_c^p = D_{ca}^{-1} K_{apm}. \quad (12)$$

Let now Z be a scalar potential and its gradient is denoted by $\mathbf{v} = \nabla Z$. The approximation of Z in \mathcal{W}_h^{N+1} is then denoted by \tilde{Z}_h , with degrees of freedom Z_q and representation

$$\tilde{Z}_h = \sum_q \psi_q(\mathbf{x}) Z_q := \psi_q Z_q \in \mathcal{W}_h^{N+1}, \quad (13)$$

while the discrete gradient is denoted by $\mathbf{v}_h \in \mathcal{U}_h^N$ and representation

$$\mathbf{v}_h = \sum_a \phi_a(\mathbf{x}) \mathbf{v}_a := \phi_a \mathbf{v}_a = \phi_a v_{ma} \in \mathcal{U}_h^N, \quad (14)$$

where the index m in v_{ma} refers to the components of the vector field \mathbf{v} and the index a to the degrees of freedom. The degrees of freedom of the discrete gradient then simply read

$$\mathbf{v}_c = \nabla_c^p Z_p = \sum_p D_{ca}^{-1} \mathbf{K}_{ap} Z_p, \quad \text{or,} \quad v_{mc} = (\partial_m)_c^p Z_p = D_{ca}^{-1} K_{apm} Z_p. \quad (15)$$

Because of the particular choice of compatible discrete function spaces \mathcal{U}_h^N and \mathcal{W}_h^{N+1} for \mathbf{v}_h and \tilde{Z}_h , respectively, this primary discrete nabla operator is *exact*, i.e. $\mathbf{v}_h = \nabla_h \tilde{Z}_h = \phi_c \nabla_c^p Z_p = \nabla \tilde{Z}_h$, with ∇ the exact nabla operator.

The discrete primary nabla operator introduced above can also be applied to general discrete vector fields $\mathbf{A}_h = \psi_q \mathbf{A}_q = \psi_q A_{kq} \in \mathcal{W}_h^{N+1}$, with k the tensor index of the physical field and q the index for the degrees of freedom:

$$\nabla_c^p \mathbf{A}_p = \sum_p D_{ca}^{-1} \mathbf{K}_{ap} \mathbf{A}_p, \quad \text{or,} \quad (\partial_m)_c^p A_{kp} = D_{ca}^{-1} K_{apm} A_{kp}. \quad (16)$$

For $N = 0$ we have $\phi_c = 1$, the inverse mass matrix is one divided by the cell volume and $\nabla \psi_p$ is the gradient of continuous P1 Lagrange FEM and we obtain the discrete primary nabla operator already used in the Lagrangian schemes [20–23, 32, 42, 72, 76–78] as a special case of our method.

The discrete primary nabla operator allows us now to rewrite the CG-DG scheme (11) in even more compact form. Multiplying (11) with the inverse of the element mass matrix yields

$$\frac{d\hat{\mathbf{u}}_c}{dt} + \nabla_c^p \cdot \hat{\mathbf{f}}_p = 0, \quad (17)$$

which for nodal basis functions ϕ_c and ψ_p could now even be interpreted as a kind of high order unstructured finite difference scheme. However, this is not the objective of this paper, but it can be related to the flux-reconstruction (FR) and spectral difference methods introduced in [33, 71, 100].

2.5.2 Discrete dual nabla operator

The discrete dual nabla operator [5] can be obtained via integration by parts

$$\begin{aligned} \int_{\Omega} \psi_p \nabla \phi_c \, d\mathbf{x} &= \int_{\Omega \setminus \mathcal{E}_h} \psi_p \nabla \phi_c \, d\mathbf{x} + \int_{\mathcal{E}_h} \psi_p (\phi_c^+ - \phi_c^-) \mathbf{n} \, dS \\ &= - \int_{\Omega} \nabla \psi_p \phi_c \, d\mathbf{x} + \int_{\partial\Omega} \psi_p \phi_c \mathbf{n} \, dS. \end{aligned} \quad (18)$$

Recall that \mathcal{E}_h denotes the skeleton of the mesh, i.e. the union of all edges (2D) or faces (3D) of all elements T_k . For suitable boundary conditions on $\partial\Omega$ one can drop the boundary contributions on $\partial\Omega$. Hence, the above expression simplifies to

$$\int_{\Omega} \psi_p \nabla \phi_c \, d\mathbf{x} = \int_{\Omega \setminus \mathcal{E}_h} \psi_p \nabla \phi_c \, d\mathbf{x} + \int_{\mathcal{E}_h} \psi_p (\phi_c^+ - \phi_c^-) \mathbf{n} \, d\mathbf{x} = - \int_{\Omega} \nabla \psi_p \phi_c \, d\mathbf{x} \quad (19)$$

which allows us to define a dual nabla operator from the DG space \mathcal{U}_h^N into the FEM space \mathcal{W}_h^{N+1} as follows:

$$\tilde{\nabla}_p^c = -\mathbf{K}_{cp}, \quad \text{or, in index notation,} \quad (\tilde{\partial}_m)_p^c = -K_{cpm}. \quad (20)$$

Note that this operator does not yet contain the multiplication by the inverse of the global finite element mass matrix

$$M_{pq} = \int_{\Omega} \psi_p \psi_q \, d\mathbf{x}. \quad (21)$$

In the case $N = 0$ we have $\phi_c = 1$, hence we recover the discrete dual nabla operator as in [20–23, 32, 42, 72, 76–78], which, however, all employ mass lumping and therefore do not require the inversion of a global mass matrix. Let Y be a scalar potential its gradient $\mathbf{g} = \nabla Y$. The approximation of Y in \mathcal{U}_h^N is denoted by Y_h , with degrees of freedom Y_a and representation

$$Y_h = \sum_a \phi_a(\mathbf{x}) Y_a := \phi_a Y_a \quad \in \mathcal{U}_h^N, \quad (22)$$

while the discrete gradient is denoted by $\tilde{\mathbf{g}}_h \in \mathcal{W}_h^{N+1}$ and with representation

$$\tilde{\mathbf{g}}_h = \sum_p \psi_p(\mathbf{x}) \mathbf{g}_p := \psi_p \mathbf{g}_p = \psi_p g_{mp} \quad \in \mathcal{W}_h^{N+1}, \quad (23)$$

where the index m in g_{mp} refers to the spatial components of the vector field and the index p to the associated degrees of freedom of the discrete solution $\tilde{\mathbf{g}}_h$. The discrete dual gradient $\tilde{\nabla}_h$ applied to Y_h reads

$$M_{pq} \mathbf{g}_q = \tilde{\nabla}_p^c Y_c = - \sum_c \mathbf{K}_{cp} Y_c, \quad \text{or,} \quad M_{pq} g_{mq} = (\tilde{\partial}_m)_p^c = -K_{cpm} Y_c. \quad (24)$$

We again provide also the discrete dual nabla operator applied to a vector field $\mathbf{A}_h = \phi_a A_{ka} \in \mathcal{U}_h^N$, with k the tensor index of the physical field and a the index for the degrees of freedom:

$$\tilde{\nabla}_p^c \mathbf{A}_c = - \sum_c \mathbf{K}_{cp} \mathbf{A}_c, \quad \text{or,} \quad (\tilde{\partial}_m)^c A_{kc} = -K_{cpm} A_{kc}. \quad (25)$$

2.6 Shock capturing via suitable artificial viscosity

In order to capture shocks and strong gradients, we employ a simple concept of artificial viscosity, which, however, is full compatible with the principles of the CG-DG scheme outlined above, in particular with the concept of a discrete flux field.

For general hyperbolic systems without involutions, the degrees of freedom of the discrete flux field are simply modified as

$$\hat{\mathbf{f}}_j = \mathbf{f}(\hat{\mathbf{u}}_j) - \epsilon_j \widehat{\nabla} \mathbf{u}_j. \quad (26)$$

Here, ϵ_j is the artificial viscosity coefficient and the $\widehat{\nabla} \mathbf{u}_j$ are the degrees of freedom of the discrete dual nabla operator applied to the DG solution \mathbf{u}_h , i.e. we have

$$\int_{\Omega} \psi_i \tilde{\nabla} \mathbf{u}_h \, d\mathbf{x} = \int_{\Omega} \psi_i \psi_j \, d\mathbf{x} \widehat{\nabla} \mathbf{u}_j = - \int_{\Omega} \nabla \psi_i \otimes \mathbf{u}_h \, d\mathbf{x}. \quad (27)$$

In this paper we simply use

$$\epsilon_j = \frac{1}{2} \chi_j \frac{h_j}{2N+1} s_j^{\max}. \quad (28)$$

with s_j^{\max} a suitable upper bound of the maximum absolute value of the eigenvalues of the hyperbolic system in all normal directions, h_j a characteristic mesh spacing and $\chi_j \in [0, 1]$ an indicator function which takes the values $\chi_j = 0$ in unlimited areas and $\chi_j = 1$ in troubled zones. For state variables in \mathbf{q} subject to involutions, the artificial viscosity specified above is not compatible and needs to be properly modified. For more details on compatible artificial viscosity, see the Section 6 below.

2.7 Comparison with classical DG schemes

In the case of a standard RK-DG scheme [35–37] one makes the same ansatz for \mathbf{u}_h as above in (2), and the weak form of the PDE reads

$$\int_{T_k} \phi_i \partial_t \mathbf{u}_h \, d\mathbf{x} + \int_{T_k} \phi_i \nabla \cdot \mathbf{f}(\mathbf{u}_h) \, d\mathbf{x} = 0, \quad \forall \phi_i \in \mathcal{U}_h^N. \quad (29)$$

But since \mathbf{u}_h and therefore also $\mathbf{f}(\mathbf{u}_h)$ is discontinuous at element boundaries, one uses a numerical flux $\hat{\mathbf{f}}(\mathbf{u}_h^-, \mathbf{u}_h^+)$, with boundary-extrapolated states \mathbf{u}_h^- and \mathbf{u}_h^+ from within

the cell and within the neighbor cell, to obtain a unique flux on the element boundary. The standard DG scheme then reads

$$\int_{T_k} \phi_i \partial_t \mathbf{u}_h d\mathbf{x} - \int_{\hat{T}_k} \nabla \phi_i \cdot \mathbf{f}(\mathbf{u}_h) d\mathbf{x} + \int_{\partial T_k} \phi_i \hat{\mathbf{f}}(\mathbf{u}_h^-, \mathbf{u}_h^+) \cdot \mathbf{n} dS = 0, \quad \forall \phi_i \in \mathcal{U}_h^N, \quad (30)$$

with $T_k^\circ = T_k \setminus \partial T_k$ the interior of the cell, or, equivalently in *fluctuation form*, after undoing integration by parts of the second term

$$\int_{T_k} \phi_i \partial_t \mathbf{u}_h d\mathbf{x} + \int_{\hat{T}_k} \phi_i \nabla \cdot \mathbf{f}(\mathbf{u}_h) d\mathbf{x} + \int_{\partial T_k} \phi_i (\hat{\mathbf{f}}(\mathbf{u}_h^-, \mathbf{u}_h^+) - \mathbf{f}(\mathbf{u}_h^-)) \cdot \mathbf{n} dS = 0, \quad \forall \phi_i \in \mathcal{U}_h^N, \quad (31)$$

which is completely different from our new CG-DG scheme (10) based on a globally continuous flux-field. In particular note that the discrete flux field in (30) is in general *not* continuous, since it is $\mathbf{f}(\mathbf{u}_h)$ inside the cell and $\hat{\mathbf{f}}(\mathbf{u}_h^-, \mathbf{u}_h^+)$ on the boundary. A 1D sketch showing this important difference between the standard DG scheme and the new CG-DG method is shown in Figure 1 below.

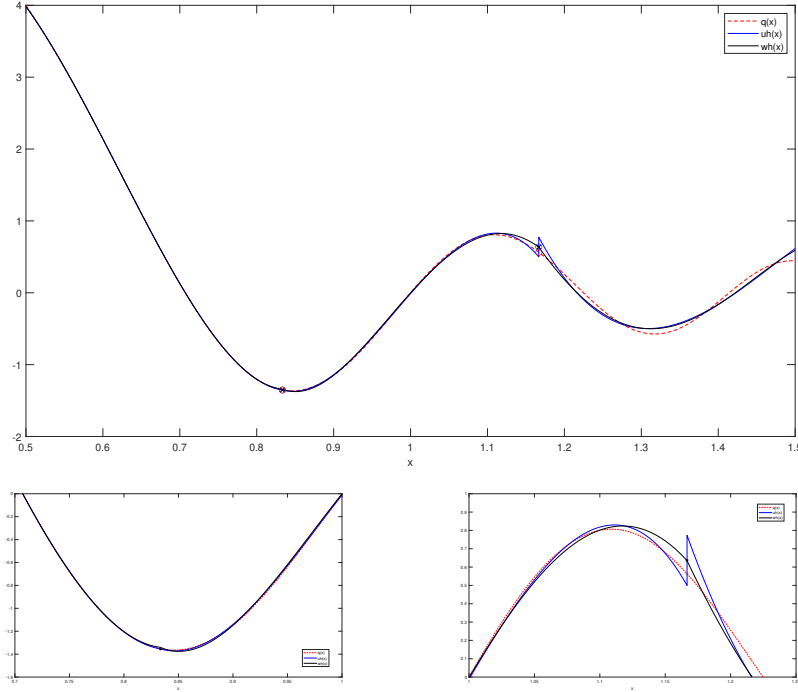


Fig. 1 Original function $q(x) = x^{-2} \sin(2\pi x^2)$, its DG approximation $u_h(x) \in \mathcal{U}_h^N$ with $N = 3$ and 3 elements on the interval $\Omega = [0.5, 1.5]$ and the continuous FEM approximation $\tilde{w}_h(x) \in \mathcal{W}_h^{N+1}$ obtained via L^2 projection (top) with two zoomed views (bottom).

3 First-order Finite Volume discretization

In this section, we explain how the method described in the previous section 2 "degenerates" when $N = 0$, i.e. when piecewise constant polynomials are used in the cells and piecewise linear approximation for the flux. We hope this will help the reader to connect to more classical settings, and also to see more clearly when and where we depart from classical settings.

3.1 Governing equations

The computational domain Ω is a subset of the Euclidean space \mathbb{R}^d , where d denotes the space dimension, which is paved with a collection of non overlapping simplex elements. Throughout this paper, $\mathbf{x} \in \mathbb{R}^d$ denotes the vector position of a point and $t > 0$ is the time. The system of conservation laws under consideration reads

$$\partial_t \mathbf{q} + \nabla \cdot \mathbf{f} = \mathbf{0}, \quad (32)$$

where $\mathbf{q} = \mathbf{q}(\mathbf{x}, t)$ is the vector of conservative variables and $\mathbf{f} = \mathbf{f}(\mathbf{q})$ the flux tensor.

It is well known that systems of conservation laws of hyperbolic type might admit multiple discontinuous solutions, refer to [57]. To select the physically admissible solutions, we supplement it with an entropy inequality. To this end, we introduce the entropy, entropy flux pair $(\mathcal{E}, \mathbf{F})$ defined by

$$\begin{aligned} \mathcal{E} : \mathbf{q} &\mapsto \mathcal{E}(\mathbf{q}) \text{ is strictly concave,} \\ \mathbf{F} : \mathbf{q} &\mapsto \mathbf{F}(\mathbf{q}) \text{ is such that, } \nabla \cdot \mathbf{F} = \partial_{\mathbf{q}} \mathcal{E} \cdot \nabla \cdot \mathbf{f}. \end{aligned}$$

Note that here, we have chosen to work with a concave entropy so that in the case of gas dynamics we recover the physical entropy. Bearing this in mind, the smooth solutions of the system of conservation laws (32) satisfy the supplementary conservation law

$$\partial_t \mathcal{E} + \nabla \cdot \mathbf{F} = 0, \quad (33)$$

whereas the admissible discontinuous, *i.e.*, weak, solutions have to fulfill the entropy inequality

$$\partial_t \mathcal{E} + \nabla \cdot \mathbf{F} > 0. \quad (34)$$

So equipped with a concave entropy, the foregoing system of conservations is assumed to be hyperbolic, that is the Jacobian matrix of the flux admits real eigenvalues and a set of linearly independent eigenvectors for all normal directions. To study the theoretical property of the subsequent finite volume discretization, it is worth defining the entropic variable, \mathbf{p} , which is nothing but the gradient of the entropy with respect to the vector of conservative variables

$$\mathbf{p} = \partial_{\mathbf{q}} \mathcal{E}. \quad (35)$$

Following Tadmor [95] we introduce the mapping

$$\mathbf{p} \mapsto \mathbf{q}(\mathbf{p}),$$

which is one-to-one by virtue of the concavity of entropy, *i.e.*, $\partial_{\mathbf{p}}\mathbf{q} = (\partial_{\mathbf{q}\mathbf{q}}\mathcal{E})^{-1} < 0$. Namely, $\mathbf{H} = \partial_{\mathbf{p}}\mathbf{q}$ is nothing but the inverse of the Hessian matrix of the entropy and is thus symmetric negative definite. Finally, we introduce the potential functions

$$\begin{aligned}\phi(\mathbf{p}) &= \langle \mathbf{p}, \mathbf{q}(\mathbf{p}) \rangle - \mathcal{E}(\mathbf{q}(\mathbf{p})), \\ \psi(\mathbf{p}) &= \mathbf{f}^\top(\mathbf{q}(\mathbf{p}))\mathbf{p} - \mathbf{F}(\mathbf{q}(\mathbf{p})),\end{aligned}$$

where $\langle \cdot, \cdot \rangle$ denotes the usual Euclidean inner product.

3.2 Finite Volume discretization

We describe the cell-centered Finite Volume discretization of the systems of conservation laws (32). To ease the notation we describe the two-dimensional discretization knowing that the three-dimensional generalization does not present any difficulties.

3.2.1 Grid notation

The two-dimensional Euclidean space is equipped with the direct orthonormal basis $(\mathbf{e}_x, \mathbf{e}_y)$ which is supplemented by $\mathbf{e}_z = \mathbf{e}_x \times \mathbf{e}_y$. The computational domain, Ω , is paved by means of a collection of nonoverlapping conformal triangles denoted ω_c and thus $\Omega = \cup_c \omega_c$. The triangular cell $\omega_c(t)$ is characterized by the set of its vertices $\mathcal{P}(c)$. The generic vertex also named point is denoted using the label p and its vector position is \mathbf{x}_p . In the counterclockwise ordered list of points of cell ω_c , the vertex p^+ is the next vertex with respect to p and p^- is the previous one. The midpoints of $[p^-, p]$ and $[p, p^+]$ are respectively $p^{-\frac{1}{2}}$ and $p^{+\frac{1}{2}}$. The quadrangle obtained joining successively the cell centroid \mathbf{x}_c to $\mathbf{x}_{p^{-\frac{1}{2}}}$, \mathbf{x}_p , $\mathbf{x}_{p^{+\frac{1}{2}}}$ and the centroid defines the subcell ω_{pc} , refer to Fig. 2-(a). The set of subcells of a given cell constitutes a partition of this cell, that is $\omega_c = \cup_{p \in \mathcal{P}(c)} \omega_{pc}$. Gathering the subcells surrounding the generic vertex p we define the dual cell, refer to Fig. 2-(b)

$$\omega_p = \bigcup_{c \in \mathcal{C}(p)} \omega_{pc}, \quad (36)$$

where $\mathcal{C}(p)$ is the set of cells sharing vertex p .

The unit outward normals to the faces of ω_c impinging at p are respectively \mathbf{n}_{pc}^- and \mathbf{n}_{pc}^+ . We also introduced the lengths of the corresponding ‘‘half-faces’’ $l_{pc}^- = \frac{1}{2}|\mathbf{x}_p - \mathbf{x}_{p^-}|$ and $l_{pc}^+ = \frac{1}{2}|\mathbf{x}_{p^+} - \mathbf{x}_p|$. The volume of the triangular cell ω_c might be expressed in terms of the position vectors of its vertices. This allows us to define the corner normal vector related to point p and cell c as the gradient of the cell volume ω_c with respect to the vector position \mathbf{x}_p

$$l_{pc}\mathbf{n}_{pc} = \frac{\partial|\omega_c|}{\partial\mathbf{x}_p}, \quad (37)$$

where $\mathbf{n}_{pc}^2 = 1$. This geometrical object is fundamental to derive staggered and cell-centered discretization of Lagrangian gas dynamics over moving grids, cf. [73] and

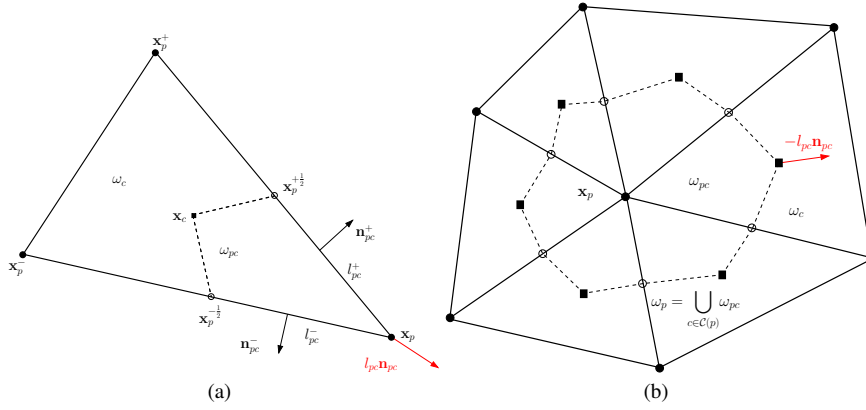


Fig. 2 Fragments of a triangular grid (a)Geometric quantities attached to the triangular cell ω_c , (b):Dual cell attached to point p .

the references therein. Computing the cell volume gradient with respect to \mathbf{x}_p yields the analytical expression of the corner normal

$$l_{pc} \mathbf{n}_{pc} = \frac{1}{2} [\mathbf{x}_{p^+}(t) - \mathbf{x}_{p^-}(t)] \times \mathbf{e}_z = l_{pc}^- \mathbf{n}_{pc}^- + l_{pc}^+ \mathbf{n}_{pc}^+. \quad (38)$$

This shows that the corner normal is the summation of the outward normals to the “half-faces” impinging at point p , refer to Fig. 2-(a). We observe that the corner normal fulfills the fundamental geometrical identity

$$\sum_{p \in \mathcal{P}(c)} l_{pc} \mathbf{n}_{pc} = \mathbf{0}. \quad (39)$$

This result, by virtue of (38), is a direct consequence of the fact that the sum of the outward normals to a closed contour is equal to zero. In [20] it was shown that the corner normal divided by the cell area $|\omega_c|$ is equal to the gradient of classical continuous P1 finite element basis functions and which establishes the link with the general method presented in the previous section for the special case $N = 0$.

The corner vector is also the cornerstone to define discrete mathematical operators such as the discrete divergence operator following the approach introduced in [92] in the more general framework of mimetic finite difference method. For any vector field $\mathbf{q} := \mathbf{q}(\mathbf{x})$, for $\mathbf{x} \in \omega_c$ we define the cell-centered discrete divergence

$$\text{DIV}_c(\mathbf{q}) = \frac{1}{|\omega_c|} \sum_{p \in \mathcal{P}(c)} \langle l_{pc} \mathbf{n}_{pc}, \mathbf{q}_p \rangle, \quad (40)$$

where $\mathbf{q}_p = \mathbf{q}(\mathbf{x}_p)$. Identity (39) implies that the divergence of constant vectors is equal to zero. Note that the discrete gradient operator over ω_c might be defined in a similar manner. The mathematical properties of the discrete operators and their application to construct numerical methods for solving different classes of partial

differential equations are described in the review paper [70]. Now, considering the dual cell ω_p , which is the union of the subcells attached to point p , refer to Fig 2, we define the discrete divergence and gradient operators of a vector as follows

$$\text{DIV}_p(\mathbf{q}) = -\frac{1}{|\omega_p|} \sum_{c \in \mathcal{C}(p)} \langle l_{pc} \mathbf{n}_{pc}, \mathbf{q}_c \rangle, \quad (41)$$

$$\text{GRAD}_p(\mathbf{q}) = -\frac{1}{|\omega_p|} \sum_{c \in \mathcal{C}(p)} l_{pc} \mathbf{q}_c \otimes \mathbf{n}_{pc}. \quad (42)$$

Here, \otimes denotes the dyadic product and $\mathbf{q} \otimes \mathbf{n}$ is the second-order tensor whose ij component in the Cartesian basis is $(\mathbf{q} \otimes \mathbf{n})_{ij} = q_i n_j$. We point out that we have used the fact that $-l_{pc} \mathbf{n}_{pc}$ is the outward normal to the contour of the dual cell ω_p .

3.2.2 Semi-discrete node-based Finite volume discretization

Let us define the cell-averaged quantity

$$\mathbf{q}_c = \frac{1}{|\omega_c|} \int_{\omega_c} \mathbf{q} \, dv.$$

Integrating the system of conservation laws (32) over ω_c and applying the Green-Gauss theorem we get

$$|\omega_c| \frac{d\mathbf{q}_c}{dt} + \int_{\partial\omega_c} \mathbf{f}(\mathbf{q}) \mathbf{n} \, ds = \mathbf{0}.$$

Employing a node-based quadrature formula for the surface integral in the foregoing equation leads us the following node-based approximation of the integral flux

$$\int_{\partial\omega_c(t)} \mathbf{f}(\mathbf{q}) \mathbf{n} \, ds = \sum_{p \in \mathcal{P}(c)} l_{pc} \mathbf{f}_p \mathbf{n}_{pc},$$

where \mathbf{f}_p is the tensor flux approximation at point p . *A priori*, \mathbf{f}_p should depend on all the states surrounding point p , namely $\mathbf{f}_p := \mathbf{f}_p(\mathbf{q}_1, \dots, \mathbf{q}_{|\mathcal{C}(p)|})$. Moreover, we assume that this multidimensional tensor flux approximation is consistent [8], that is when $\mathbf{q}_c = \mathbf{q}$ for all $c \in \mathcal{C}(p)$ then $\mathbf{f}_p(\mathbf{q}, \dots, \mathbf{q}) = \mathbf{f}(\mathbf{q})$. Gathering the previous definition we arrive at the node-based Finite Volume discretization of the system of conservation laws (32)

$$|\omega_c| \frac{d\mathbf{q}_c}{dt} + \sum_{p \in \mathcal{P}(c)} l_{pc} \mathbf{f}_p \mathbf{n}_{pc} = \mathbf{0}. \quad (43)$$

We observe that this scheme is conservative by construction by virtue of the geometrical identity (39) and since the corner normal divided by the cell volume is the gradient of the continuous finite element P1 basis functions the above scheme is identical with (10) for the special case $N = 0$. In addition, it is worth noting that the present Finite Volume scheme might be recasted under the form of the following Residual Distribution scheme

$$|\omega_c| \frac{d\mathbf{q}_c}{dt} + \sum_{p \in \mathcal{P}(c)} \Phi_c^p = \mathbf{0}, \quad (44)$$

where the corner fluctuation Φ_c^p reads

$$\Phi_c^p = l_{pc} [\mathbf{f}_p - \mathbf{f}(\mathbf{q}_c)] \mathbf{n}_{pc}.$$

3.2.3 Structural form of the node-based multidimensional flux

We derive the structural form of the node-based multidimensional flux, \mathbf{f}_p , so that a semi-discrete entropy inequality is ensured. First, the semi-discrete equation satisfied by the entropy cell-averaged results from taking the dot product of (44) by \mathbf{p}_c

$$|\omega_c| \frac{d\mathcal{E}(\mathbf{q}_c)}{dt} + \sum_{p \in \mathcal{P}(c)} \langle \Phi_c^p, \mathbf{p}_c \rangle = 0.$$

Let us develop the term between brackets in the foregoing equation expressing the corner fluctuation in terms of the nodal flux

$$\langle \Phi_c^p, \mathbf{p}_c \rangle = \langle l_{pc} [\mathbf{f}_p - \mathbf{f}(\mathbf{q}_c)] \mathbf{n}_{pc}, \mathbf{p}_c \rangle = \langle l_{pc} \mathbf{f}_p \mathbf{n}_{pc}, \mathbf{p}_c \rangle + \langle l_{pc} \mathbf{f}^\top(\mathbf{q}_c) \mathbf{p}_c, \mathbf{n}_{pc} \rangle. \quad (45)$$

Before proceeding further, let us recall some useful mathematical notation. For any second-order tensor \mathbf{A} and any pair of vectors (\mathbf{n}, \mathbf{p}) , one has

$$\langle \mathbf{A} \mathbf{n}, \mathbf{p} \rangle = \text{Tr}(\mathbf{A} \mathbf{n} \otimes \mathbf{p}) = \text{Tr}(\mathbf{A}(\mathbf{n} \otimes \mathbf{p})) = \mathbf{A} : (\mathbf{p} \otimes \mathbf{n}). \quad (46)$$

Here, $\text{Tr}()$ denotes the trace operator and $:$ the inner product of second-order tensors. These quantities are defined as follows [59]: $\text{Tr}(\mathbf{A}) = \sum_{i=1 \dots d} A_{ii}$, where A_{ij} denotes the ij component of \mathbf{A} in the Cartesian basis; and, for any second-order tensor \mathbf{B} , the inner product between \mathbf{A} and \mathbf{B} is given by $\mathbf{A} : \mathbf{B} = \text{Tr}(\mathbf{A}^\top \mathbf{B})$.

Bearing this in mind, (45) turns into

$$\langle \Phi_c^p, \mathbf{p}_c \rangle = l_{pc} \mathbf{f}_p : (\mathbf{p}_c \otimes \mathbf{n}_{pc}) - \langle l_{pc} (\psi_c + \mathbf{F}_c), \mathbf{n}_{pc} \rangle,$$

by virtue of the definition of the potential function ψ . Summing the foregoing expression over all the cells surrounding point p we get

$$\begin{aligned} \sum_{c \in \mathcal{C}(p)} \langle \Phi_c^p, \mathbf{p}_c \rangle &= \mathbf{f}_p : \sum_{c \in \mathcal{C}(p)} l_{pc} (\mathbf{p}_c \otimes \mathbf{n}_{pc}) - \sum_{c \in \mathcal{C}(p)} \langle l_{pc} \psi_c, \mathbf{n}_{pc} \rangle - \sum_{c \in \mathcal{C}(p)} \langle l_{pc} \mathbf{F}_c, \mathbf{n}_{pc} \rangle \\ &= -|\omega_p| [\mathbf{f}_p : \text{GRAD}_p(\mathbf{p}) - \text{DIV}_p(\psi)] - \sum_{c \in \mathcal{C}(p)} \langle l_{pc} \mathbf{F}_c, \mathbf{n}_{pc} \rangle. \end{aligned} \quad (47)$$

Here, we have introduced the discrete gradient and divergence operators defined over the dual cell ω_p according to (41) and (42). Finally, we observe that the entropy consistency condition at the node [8]

$$\sum_{c \in \mathcal{C}(p)} \langle l_{pc} \Phi_c^p, \mathbf{p}_c \rangle \leq - \sum_{c \in \mathcal{C}(p)} \langle l_{pc} \mathbf{F}_c, \mathbf{n}_{pc} \rangle, \quad (48)$$

is fulfilled if and only

$$\mathbf{f}_p : \text{GRAD}_p(\mathbf{p}) - \text{DIV}_p(\psi) \geq 0. \quad (49)$$

The latter inequality can be interpreted as the multidimensional extension of Tadmor's condition [95] for defining an entropy-stable flux in the one-dimensional case. A

sufficient condition for satisfying (49) is obtained by introducing the following *ansatz* for the multidimensional flux:

$$\mathbf{f}_p = \{\mathbf{f}\}_p - \frac{1}{2}\varepsilon_p h_p a_p \mathbf{H}_p \text{GRAD}_p(\mathbf{p}). \quad (50)$$

Here, $\{\mathbf{f}\}_p$ denotes some average defined at point p of the cell values of the tensor flux, $\varepsilon_p > 0$ is a viscosity coefficient, h_p is a length at node p , $a_p > 0$ is a characteristic velocity at point p and \mathbf{H}_p is the Hessian matrix evaluated at point p . With this expression of the multidimensional flux we arrive at

$$\mathbf{f}_p : \text{GRAD}_p(\mathbf{p}) - \text{DIV}_p(\boldsymbol{\psi}) = \{\mathbf{f}\}_p : \text{GRAD}_p(\mathbf{p}) - \text{DIV}_p(\boldsymbol{\psi}) - \frac{1}{2}\varepsilon_p h_p a_p \mathbf{H}_p \text{GRAD}_p(\mathbf{p}) : \text{GRAD}_p(\mathbf{p}).$$

The last term in the right-hand side of the foregoing equation is positive by virtue of the negative definiteness of \mathbf{H}_p . Indeed, $-\mathbf{H}_p$ is symmetric positive definite and we can compute its square root, \mathbf{S}_p , which satisfies $\mathbf{S}^2 = -\mathbf{H}_p$ and then

$$\begin{aligned} -\mathbf{H}_p \text{GRAD}_p(\mathbf{p}) : \text{GRAD}_p(\mathbf{p}) &= \text{Tr} [\text{GRAD}_p^\top(\mathbf{p}) \mathbf{S}_p \mathbf{S}_p \text{GRAD}_p^\top(\mathbf{p})] \\ &= \text{Tr} [(\mathbf{S}_p \text{GRAD}_p(\mathbf{p}))^\top \mathbf{S}_p \text{GRAD}_p(\mathbf{p})] \\ &= (\mathbf{S}_p \text{GRAD}_p(\mathbf{p})) : (\mathbf{S}_p \text{GRAD}_p(\mathbf{p})) \geq 0. \end{aligned}$$

Finally, to achieve the control of the sign of the left-hand side of the multidimensional Tadmors' condition, we supplement the expression of the multidimensional nodal flux as follows

$$\mathbf{f}_p = \{\mathbf{f}\}_p - \frac{1}{2}\varepsilon_p h_p a_p \mathbf{H}_p \text{GRAD}_p(\mathbf{p}) + \alpha_p \mathbf{H}_p \text{GRAD}_p(\mathbf{p}). \quad (51)$$

Here, the coefficient α_p is chosen so that the latter supplementary term cancels exactly with $\{\mathbf{f}\}_p : \text{GRAD}_p(\mathbf{p}) - \text{DIV}_p(\boldsymbol{\psi})$

$$\alpha_p = - \frac{\{\mathbf{f}\}_p : \text{GRAD}_p(\mathbf{p}) - \text{DIV}_p(\boldsymbol{\psi})}{\mathbf{H}_p \text{GRAD}_p(\mathbf{p}) : \text{GRAD}_p(\mathbf{p})}.$$

4 Properties of the method

Now we come back to the general case described in Section 2.

4.1 Basic properties

We first recall two basic properties of the primary discrete nabla operator, as already discussed in [5]. The continuous finite element space \mathcal{W}_h^{N+1} is *globally continuous*, hence it is obvious that all *tangential derivatives*, i.e. the tangential components of the gradient, are *continuous* across elements. We also stress again that the two ansatz spaces \mathcal{U}_h^N and \mathcal{W}_h^{N+1} are deliberately chosen in such a way that the DG space \mathcal{U}_h^N is rich enough to represent all first derivatives (the full gradient) of a function represented in the finite element space \mathcal{W}_h^{N+1} *exactly*. We therefore can state the

Proposition 1 For any discrete scalar field $\tilde{Z}_h \in \mathcal{W}_h^{N+1}$ and any pair of elements T_b and T_c the jump of the tangential derivatives vanishes across the common edge / face $\partial T_{bc} = T_b \cap T_c$, i.e.

$$(\nabla \tilde{Z}_h^+ - \nabla \tilde{Z}_h^-) \cdot \mathbf{t} = 0, \quad (52)$$

with \mathbf{t} all vectors tangential to ∂T_{bc} and \tilde{Z}_h^+ , \tilde{Z}_h^- the boundary-extrapolated values of \tilde{Z}_h seen from elements T_b and T_c , respectively.

Proof Due to the global continuity of $\tilde{Z}_h \in \mathcal{W}_h^{N+1}$ one has clearly

$$\tilde{Z}_h^+ = \tilde{Z}_h^-, \quad \text{or, equivalently} \quad \tilde{Z}_h^+ - \tilde{Z}_h^- = 0, \quad \forall \mathbf{x} \in \partial T_{bc}.$$

It is therefore obvious that for all vectors \mathbf{t} tangential to ∂T_{bc} one has

$$\frac{\partial \tilde{Z}_h^+}{\partial \mathbf{t}} = \frac{\partial \tilde{Z}_h^-}{\partial \mathbf{t}}, \quad \text{or, equivalently} \quad (\nabla \tilde{Z}_h^+ - \nabla \tilde{Z}_h^-) \cdot \mathbf{t} = 0, \quad \forall \mathbf{x} \in \partial T_{bc}.$$

As direct consequence of Proposition 1 we also immediately have the property that the normal component of the curl of a vector field $\tilde{\mathbf{A}}_h \in \mathcal{W}_h^{N+1}$ is continuous across elements.

Proposition 2 For any discrete vector field $\tilde{\mathbf{A}}_h \in \mathcal{W}_h^{N+1}$ and any pair of elements T_b and T_c the jump of the normal component of the curl vanishes across the common edge / face $\partial T_{bc} = T_b \cap T_c$, i.e.

$$(\nabla \times \tilde{\mathbf{A}}_h^+ - \nabla \times \tilde{\mathbf{A}}_h^-) \cdot \mathbf{n} = 0, \quad (53)$$

with \mathbf{n} the unit normal vector of ∂T_{bc} pointing from T_c to T_b and $\tilde{\mathbf{A}}_h^+$, $\tilde{\mathbf{A}}_h^-$ the boundary-extrapolated values of $\tilde{\mathbf{A}}_h$ seen from elements T_b and T_c , respectively.

Proof The proof becomes easier when using the Einstein index notation, i.e. here we will denote the components of the vector field $\tilde{\mathbf{A}}_h$ by \tilde{A}_p and drop the subscript h to ease notation.

Furthermore, the components of the tangential vectors \mathbf{t} will be denoted by t_k and those of the unit normal vector \mathbf{n} by n_k . Due to the global continuity of $\tilde{\mathbf{A}}_h \in \mathcal{W}_h^{N+1}$ one has clearly componentwise

$$\tilde{A}_p^+ = \tilde{A}_p^-, \quad \text{or} \quad \tilde{A}_p^+ - \tilde{A}_p^- = 0, \quad \forall \mathbf{x} \in \partial T_{bc}.$$

It is therefore obvious that for all vectors \mathbf{t} tangential to ∂T_{bc} one has componentwise

$$(\partial_j \tilde{A}_p^+ - \partial_j \tilde{A}_p^-) t_j = 0, \quad \forall \mathbf{x} \in \partial T_{bc}.$$

Hence, in general, the only non-vanishing component of the jump in the gradient of $\tilde{\mathbf{A}}_h$ at the element boundary ∂T_{bc} is the jump of the derivative in the normal direction, i.e.

$$(\partial_j \tilde{A}_p^+ - \partial_j \tilde{A}_p^-) = \partial_j (\tilde{A}_p^+ - \tilde{A}_p^-) = \partial_m (\tilde{A}_p^+ - \tilde{A}_p^-) n_m n_j.$$

Using the above result and the usual fully antisymmetric Levi-Civita tensor ϵ_{ijk} in Einstein index notation it is now easy to see that

$$(\nabla \times \tilde{\mathbf{A}}_h^+ - \nabla \times \tilde{\mathbf{A}}_h^-) \cdot \mathbf{n} = \epsilon_{ijk} (\partial_j \tilde{A}_k^+ - \partial_j \tilde{A}_k^-) n_i = \epsilon_{ijk} (\partial_m \tilde{A}_k^+ - \partial_m \tilde{A}_k^-) n_m n_i n_j = 0,$$

since the contraction of the anti-symmetric Levi-Civita tensor with the symmetric tensor $n_i n_j$ vanishes, i.e. $\epsilon_{ijk} n_i n_j = 0$.

4.2 Discrete Schwarz theorem and resulting discrete vector calculus identities

As already shown in [5], the two discrete nabla operators introduced before satisfy a discrete Schwarz theorem. To make this paper self-contained and to facilitate the reader, here we briefly summarize the main findings of [5]. The essential key feature of the two nabla operators is that they satisfy a discrete version of the Schwarz theorem. Then, as a direct consequence, the two discrete vector calculus identities follow automatically.

Theorem 1 *The two discrete nabla operators (12) and (20) satisfy the following discrete Schwarz theorem*

$$(\tilde{\partial}_j)_p^c (\partial_k)_c^q Z_q = (\tilde{\partial}_k)_p^c (\partial_j)_c^q Z_q. \quad (54)$$

Proof For clarity we use the Einstein index notation. From the definitions (12) and (20) we have

$$\begin{aligned} (\tilde{\partial}_j)_p^c (\partial_k)_c^q Z_q &= - \int_{\Omega} \nabla \psi_p \nabla \tilde{Z}_h \, d\mathbf{x} \\ &= \int_{\Omega \setminus \mathcal{E}_h} \psi_p \partial_j \partial_k \tilde{Z}_h \, d\mathbf{x} + \int_{\mathcal{E}_h} \psi_p (\partial_k \tilde{Z}_h^+ - \partial_k \tilde{Z}_h^-) n_j \, dS, \end{aligned} \quad (55)$$

with \mathcal{E}_h the skeleton of the mesh. Since \tilde{Z}_h is smooth inside each simplex T_k , the classical continuous Schwarz theorem obviously holds, $\partial_j \partial_k \tilde{Z}_h = \partial_k \partial_j \tilde{Z}_h$, and due to the global continuity of \tilde{Z}_h across element edges / faces $\nabla \tilde{Z}_h$ is allowed to jump across \mathcal{E}_h only in the normal direction and not in the tangential directions, hence also the jump term, which can be rewritten as

$$(\partial_k \tilde{Z}_h^+ - \partial_k \tilde{Z}_h^-) n_j = (\partial_m \tilde{Z}_h^+ - \partial_m \tilde{Z}_h^-) n_m n_k n_j = (\partial_j \tilde{Z}_h^+ - \partial_j \tilde{Z}_h^-) n_k$$

is clearly symmetric in the indices j and k . Hence, the discrete Schwarz theorem follows:

$$\begin{aligned} (\tilde{\partial}_j)_p^c (\partial_k)_c^q Z_q &= \int_{\Omega \setminus \mathcal{E}_h} \psi_p \partial_j \partial_k \tilde{Z}_h \, d\mathbf{x} + \int_{\mathcal{E}_h} \psi_p (\partial_k \tilde{Z}_h^+ - \partial_k \tilde{Z}_h^-) n_j \, dS \\ &= \int_{\Omega \setminus \mathcal{E}_h} \psi_p \partial_k \partial_j \tilde{Z}_h \, d\mathbf{x} + \int_{\mathcal{E}_h} \psi_p (\partial_j \tilde{Z}_h^+ - \partial_j \tilde{Z}_h^-) n_k \, dS = (\tilde{\partial}_k)_p^c (\partial_j)_c^q Z_q. \end{aligned} \quad (56)$$

As consequence we have

Corollary 1 *The two discrete nabla operators (12) and (20) satisfy a discrete Schwarz theorem also for discrete vector fields*

$$(\tilde{\partial}_j)_p^c (\partial_k)_c^q A_{mq} = (\tilde{\partial}_k)_p^c (\partial_j)_c^q A_{mq}. \quad (57)$$

Proof Replacing Z_q by A_{mq} in the proof of the previous Theorem (1) leads immediately to the result.

Theorem 2 Given the two discrete nabla operators (12) and (20), a discrete scalar potential $\tilde{Z}_h \in \mathcal{W}_h^{N+1}$ with degrees of freedom $Z_q \in \mathbb{R}$ and a discrete vector potential $\tilde{\mathbf{A}}_h \in \mathcal{W}_h^{N+1}$ with degrees of freedom $\mathbf{A}_q \in \mathbb{R}^3$ and representation

$$\tilde{Z}_h = \psi_q Z_q \in \mathcal{W}_h^{N+1}, \quad \tilde{\mathbf{A}}_h = \psi_q \mathbf{A}_q \in \mathcal{W}_h^{N+1}, \quad (58)$$

then the following discrete vector calculus identities hold:

$$\tilde{\nabla}_p^c \times (\nabla_c^q Z_q) = 0, \quad (59)$$

and

$$\tilde{\nabla}_p^c \cdot (\nabla_c^q \times \mathbf{A}_q) = 0. \quad (60)$$

Proof We employ Einstein index notation for convenience and also make use of the classical fully antisymmetric Levi-Civita tensor ϵ_{ijk} , which is well-known and whose definition does not need to be repeated here. The identity (59) is easily proven at the aid of the definition of the curl and of the divergence in index notation

$$\tilde{\nabla}_p^c \times \nabla_c^q Z_q = \epsilon_{ijk} (\tilde{\partial}_j)_p^c (\partial_k)_c^q Z_q = 0. \quad (61)$$

The result of the expression on the left hand side is zero, because the contraction of the antisymmetric Levi-Civita symbol ϵ_{ijk} with a symmetric tensor is zero. The tensor $(\tilde{\partial}_j)_p^c (\partial_k)_c^q Z_q$ is symmetric thanks to the discrete Schwarz theorem (56) above. The second identity (60) can be proven in the same manner:

$$\tilde{\nabla}_p^c \cdot \nabla_c^q \times \mathbf{A}_q = (\tilde{\partial}_i)_p^c \epsilon_{ijk} (\partial_j)_c^q A_{kq} = 0, \quad (62)$$

The expression on the left hand side is zero for the same reasons as before, i.e. simply using (12) and (20) in index notation, the discrete Schwarz theorem for vector fields (57) and using the fact that the contraction of the antisymmetric Levi-Civita symbol with a symmetric tensor is zero.

Correct choice of initial data In order to guarantee that divergence and curl involutions hold exactly at the discrete level, please note that the discrete solution in the DG space \mathcal{U}_h^N cannot be simply initialized via classical element-local L^2 projection. Instead, the initial condition for those state variables in the DG space \mathcal{U}_h^N that have to satisfy involution constraints must necessarily be also properly computed as the discrete gradient or discrete curl of the corresponding discrete scalar or vector potentials in the continuous finite element space \mathcal{W}_h^{N+1} . As an example, a discretely divergence-free magnetic field $\mathbf{B}_h \in \mathcal{U}_h^N$ must be initialized as

$$\mathbf{B}_h(\mathbf{x}, 0) = \nabla \times \tilde{\mathbf{A}}_h(\mathbf{x}, 0), \quad (63)$$

with a discrete vector potential $\tilde{\mathbf{A}}_h(\mathbf{x}, 0) \in \mathcal{W}_h^{N+1}$. For the degrees of freedom of $\mathbf{B}_h(\mathbf{x}, 0)$ at the initial time we simply get

$$\mathbf{B}_c(0) = \nabla_c^q \times \mathbf{A}_q(0). \quad (64)$$

Likewise, to initialize for example a discretely curl-free velocity field $\mathbf{v}_h \in \mathcal{U}_h^N$, one must compute it as the gradient of a discrete scalar potential $\tilde{Z}_h \in \mathcal{W}_h^{N+1}$, i.e.

$$\mathbf{v}_h(\mathbf{x}, 0) = \nabla \tilde{Z}_h(\mathbf{x}, 0), \quad (65)$$

or, in terms of the degrees of freedom

$$\mathbf{v}_c(0) = \nabla_c^q Z_q(0). \quad (66)$$

4.3 Exact pointwise local conservation and preservation of involutions.

Let us again consider the scheme (10) that we rewrite as for all elements T_k

$$\int_{T_k} \phi_i (\partial_t \mathbf{u}_h + \nabla \cdot \tilde{\mathbf{f}}_h) \, d\mathbf{x} = 0. \quad (67)$$

Here $\mathbf{u}_h \in \mathcal{U}_h^N$ and $\tilde{\mathbf{f}}_h \in \mathcal{W}_h^{N+1}$. Clearly, $\nabla \cdot \tilde{\mathbf{f}}_h \in \mathcal{U}_h^N$, so that we have, **strongly** on each T_k ,

$$\partial_t \mathbf{u}_h + \nabla \cdot \tilde{\mathbf{f}}_h = 0. \quad (68)$$

This shows pointwise conservation in each element. Local conservation is guaranteed because for each element, the characteristic function of T_k belongs to \mathcal{U}_h^N , i.e.

$$\int_{T_k} \partial_t \mathbf{u}_h \, d\mathbf{x} + \int_{T_k} \nabla \cdot \tilde{\mathbf{f}}_h \, d\mathbf{x} = 0,$$

and using again the continuity of $\tilde{\mathbf{f}}_h$ across the boundary of T_i , we get

$$\frac{d}{dt} \int_{T_k} \mathbf{u}_h \, d\mathbf{x} + \int_{\partial T_k} \tilde{\mathbf{f}}_h \cdot \mathbf{n} \, d\gamma = 0. \quad (69)$$

We now show that

Proposition 3 *For any volume V included in Ω , we have the conservation relation:*

$$\frac{d}{dt} \int_V \mathbf{u}_h \, d\mathbf{x} + \int_{\partial V} \tilde{\mathbf{f}}_h \cdot \mathbf{n} \, d\gamma. \quad (70)$$

This relation is more general than the usual one because the volume V can be arbitrary.

Proof Since $\tilde{\mathbf{f}}_h \in \mathcal{W}_h^{N+1} \subset H^1(\Omega)$, $\nabla \cdot \tilde{\mathbf{f}}_h \in L^2(\Omega)$ and writing

$$V = \cup_k (V \cap T_k),$$

we get from (68)

$$\frac{d}{dt} \int_V \mathbf{u}_h \, d\mathbf{x} + \sum_{T_k} \int_{V \cap T_k} \nabla \cdot \tilde{\mathbf{f}}_h \, d\mathbf{x} = 0.$$

Then,

$$\int_{V \cap T_k} \nabla \cdot \tilde{\mathbf{f}}_h \, d\mathbf{x} = \int_{\partial(V \cap T_k)} \tilde{\mathbf{f}}_h \cdot \mathbf{n} \, d\gamma.$$

The boundary $\partial(V \cap T_k)$ has two parts: one part that is contained in the skeleton of the mesh, and a part that is made of edges or two dimensional flat pieces that are contained in the interior of the triangles. We will call this second part in the following the second skeleton. Because of the continuity of the reconstructed flux $\tilde{\mathbf{f}}_h$,

the contribution on the skeleton vanishes. The union of the pieces contained in the second skeleton is simply ∂V , so that in the end

$$\sum_{T_k} \int_{V \cap T_k} \nabla \cdot \tilde{\mathbf{f}}_h \, d\mathbf{x} = \int_{\partial V} \mathbf{f}^h \cdot \mathbf{n} \, d\gamma.$$

This ends the proof of Proposition (3).

Thanks to (67), we also respect involutions everywhere. Assume that the system (1) satisfies the involution

$$\frac{d}{dt} \operatorname{curl} L(\mathbf{q}) = 0$$

where L is a linear operator. This means that (1) satisfies

$$\operatorname{curl}(L(\nabla \cdot \mathbf{f})) = 0$$

or in other words that

$$L(\nabla \cdot \mathbf{f}) = \nabla G(\mathbf{q})$$

for some functional G . Similarly, we could have involutions of the kind

$$\frac{d}{dt} \operatorname{div} L(\mathbf{q}) = 0$$

i.e.

$$\operatorname{div}(L(\nabla \cdot \mathbf{f})) = 0$$

that is that

$$L(\nabla \cdot \mathbf{f}) = \operatorname{curl} G(\mathbf{q})$$

for some G . Typical examples are:

- For the acoustic equations, where $\mathbf{q} = (\mathbf{v}, p)^T$, the operator L is $L(\mathbf{q}) = \mathbf{v}$ and then $G(\mathbf{q}) = \nabla p$
- For the Maxwell equations $\mathbf{q} = (\mathbf{E}, \mathbf{B})^T$, the we may consider

$$L(\mathbf{q}) = \mathbf{E} \text{ or } L(\mathbf{q}) = \mathbf{B}$$

so that $G(\mathbf{q}) = \operatorname{curl} \mathbf{E}$ or $G(\mathbf{q}) = -\operatorname{curl} \mathbf{B}$

What matters is that $L(\nabla \cdot \tilde{\mathbf{f}}_h) = \nabla \cdot \tilde{G}_h$ in the first case and that $L(\nabla \cdot \tilde{\mathbf{f}}_h) = \operatorname{curl} \tilde{G}_h$ in the second case. This is true for the two examples given previously. Using (67), we see that pointwise, we will have

$$\frac{d}{dt} \operatorname{curl} L(\mathbf{q}_h) = 0 \quad \text{or} \quad \frac{d}{dt} \operatorname{div} L(\mathbf{q}_h) = 0.$$

The question now is what happens across the edges and faces.

- For the curl operator. We need that whatever τ normal to the face f , $L(\mathbf{q}) \cdot \tau$ is continuous across f . More precisely, we show that for any polynomial p_N of degree N ,

$$\frac{d}{dt} \int_f p_N [L(\mathbf{q}) \cdot \tau] \, d\gamma = 0.$$

Proof The face f is the intersection of two elements, T and T' . Since from T , we have

$$\begin{aligned} \frac{d}{dt} \int_{f \cap T} p_N L(\mathbf{q}_h) \cdot \boldsymbol{\tau} \, d\gamma &= \int_{f \cap T} p_N \left(\frac{d}{dt} L(\mathbf{q}_h) \right) \cdot \boldsymbol{\tau} \, d\gamma = - \int_{f \cap T} p_N \nabla \tilde{\mathbf{G}}_h \cdot \boldsymbol{\tau} \\ &= - \int_{f \cap T} p_N \partial_\tau \tilde{\mathbf{G}}_h \end{aligned}$$

Seen from T' , we have

$$\frac{d}{dt} \int_{f \cap T'} p_N L(\mathbf{q}_h) \cdot \boldsymbol{\tau} \, d\gamma = - \int_{f \cap T'} p_N \partial_\tau \tilde{\mathbf{G}}_h$$

Since $\partial_\tau \tilde{\mathbf{G}}_h$ is continuous across f , we then see that

$$0 = \frac{d}{dt} \int_f p_N [L(\mathbf{q}) \cdot \boldsymbol{\tau}] \, d\gamma = \int_f p_N \frac{d}{dt} [L(\mathbf{q}) \cdot \boldsymbol{\tau}] \, d\gamma$$

Because $[L(\mathbf{q}) \cdot \boldsymbol{\tau}]$ is a polynomial of degree N , this means that pointwise, we have

$$\frac{d}{dt} [L(\mathbf{q}) \cdot \boldsymbol{\tau}] = 0$$

– For the divergence operator, we can also show that

$$\frac{d}{dt} \int_f p_N [L(\mathbf{q}) \cdot \mathbf{n}] \, d\gamma = 0.$$

The proof is similar and comes from

$$p_N \operatorname{curl} \tilde{\mathbf{G}} \cdot \mathbf{n} = p_N \operatorname{div} (\tilde{\mathbf{G}} \times \mathbf{n})$$

Then using coordinates in the orthogonal frame $\{\mathbf{n}, \boldsymbol{\tau}_1, \boldsymbol{\tau}_2\}$ where $\boldsymbol{\tau}_1, \boldsymbol{\tau}_2$ is a basis of the face, we first write $\mathbf{G} = (G_n, G_{\tau_1}, G_{\tau_2})$ and see that

$$\mathbf{G} \times \mathbf{n} = \begin{pmatrix} 0 \\ -G_{\tau_2} \\ G_{\tau_1} \end{pmatrix}$$

and then

$$\operatorname{div} (\mathbf{G} \times \mathbf{n}) = -\partial_{\tau_1} G_{\tau_2} + \partial_{\tau_2} G_{\tau_1}$$

and this quantity, on the face, only depend on the τ_1 and τ_2 coordinate since the \mathbf{n} coordinate is constant. This shows that $[L(\mathbf{q}) \cdot \mathbf{n}]$ is constant because it is a polynomial of degree N .

We have shown the following

Proposition 4 *Assume that the system $\partial_t \mathbf{q} + \nabla \cdot \mathbf{f} = 0$ admit the involution*

$$\frac{d}{dt} \operatorname{curl} L(\mathbf{q}) = 0 \text{ or } \frac{d}{dt} \operatorname{div} L(\mathbf{q}) = 0$$

i.e. $L(\nabla \cdot \mathbf{f}) = \nabla \cdot \mathbf{G}$ or $L(\nabla \cdot \mathbf{f}) = \operatorname{curl} \mathbf{G}$ for a suitable \mathbf{G} . If we have $L(\nabla \cdot \tilde{\mathbf{f}}) = \nabla \cdot \tilde{\mathbf{G}}$ or $L(\nabla \cdot \tilde{\mathbf{f}}) = \operatorname{curl} \tilde{\mathbf{G}}$, then the scheme respects pointwise the involution.

4.4 Relation with the continuous finite element method

We assume that $\mathbf{\Pi}_h$ and π_h are L^2 projections on \mathcal{W}_h^{N+1} and \mathcal{U}_h^N respectively. With this assumption, the reconstructed variable $\tilde{\mathbf{w}}_h$ solves a standard continuous finite element discretization.

Lemma 1 *Let \mathbf{u}_h be the solution of (10) and define $\tilde{\mathbf{w}}_h \doteq \mathbf{\Pi}_h \mathbf{u}_h$. Then $\tilde{\mathbf{w}}_h$ is the solution to the standard Continuous Galerkin problem: find $\tilde{\mathbf{w}}_h \in \mathcal{W}_h^{N+1}$ such that*

$$\int_{\Omega} \partial_t \tilde{\mathbf{w}}_h \psi_i \, d\mathbf{x} - \int_{\Omega} \tilde{\mathbf{f}}_h \cdot \nabla \psi_i \, d\mathbf{x} = 0, \quad \forall \psi_i \in \mathcal{W}_h^{N+1}, \quad (71)$$

subject to the initial condition $\tilde{\mathbf{w}}_h(0) = \mathbf{\Pi}_h \mathbf{u}_h(0)$.

Proof We chose the test function $\phi_i = \pi_h \psi_i$ in (10) with $\psi_i \in \mathcal{W}_h^{N+1}$. Since $\nabla \cdot \tilde{\mathbf{f}}_h \in \mathcal{U}_h^N$ and π_h is self-adjoint with respect to the L^2 product, we obtain

$$\begin{aligned} 0 &= \int_{\Omega} \partial_t \mathbf{u}_h \cdot \pi_h \psi_i \, d\mathbf{x} + \int_{\Omega} \nabla \cdot \tilde{\mathbf{f}}_h \pi_h \psi_i \, d\mathbf{x} \\ &= \int_{\Omega} \partial_t (\pi_h \mathbf{u}_h) \psi_i \, d\mathbf{x} + \int_{\Omega} (\pi_h \nabla \cdot \tilde{\mathbf{f}}_h) \psi_i \, d\mathbf{x} \\ &= \int_{\Omega} \partial_t \mathbf{u}_h \psi_i \, d\mathbf{x} + \int_{\Omega} \nabla \cdot \tilde{\mathbf{f}}_h \psi_i \, d\mathbf{x} \\ &= \int_{\Omega} \partial_t (\mathbf{\Pi}_h \mathbf{u}_h) \psi_i \, d\mathbf{x} + \int_{\Omega} \nabla \cdot \tilde{\mathbf{f}}_h \psi_i \, d\mathbf{x}. \end{aligned}$$

The proof is concluded with the definition $\tilde{\mathbf{w}}_h \doteq \mathbf{\Pi}_h \mathbf{u}_h$ and integration by parts.

Remark 1 Even though our method is equivalent to a standard continuous Galerkin method, what makes it unique and novel is the initialization $\tilde{\mathbf{w}}_h(0) = \mathbf{\Pi}_h \mathbf{u}_h(0)$, which guarantees both exact pointwise conservation and involution preservation for the variable \mathbf{u}_h .

4.5 Quadratic energy conservation, nonlinear stability and error estimates for linear symmetric hyperbolic systems

In this section, we assume that $\mathbf{f}(\mathbf{q}) = \mathbf{A}\mathbf{q}$ with $\mathbf{A} = A_{ijk}$ is a constant tensor of rank 3, **symmetric** in the first two components, so that (1) can be written in index notation as

$$\partial_t q_i + A_{ijk} \partial_k q_j = 0. \quad (72)$$

Note that the symmetry implies the integration-by-parts formula

$$\int_{\Omega} \nabla \cdot (\mathbf{A}(\mathbf{q} \otimes \mathbf{p})) \, d\mathbf{x} = \int_{\Omega} (\mathbf{A} : \nabla \mathbf{q}) \mathbf{p} \, d\mathbf{x} + \int_{\Omega} \mathbf{q} \cdot (\mathbf{A} : \nabla \mathbf{p}) \, d\mathbf{x}, \quad (73)$$

for smooth vector fields \mathbf{q} and \mathbf{p} . For the ease of notation we introduce the L^2 norm of a vector field \mathbf{q} as

$$\|\mathbf{q}\| \doteq \sqrt{\int_{\Omega} |\mathbf{q}|^2 dx}.$$

Then, we readily obtain conservation of energy.

Lemma 2 (Continuous energy conservation) *Let \mathbf{q} be the exact solution of (73). If \mathbf{q} is sufficiently smooth and vanishes on the boundary of Ω , then it satisfies the energy conservation*

$$\frac{1}{2} \partial_t \|\mathbf{q}\|^2 = 0. \quad (74)$$

Proof Multiply (72) by \mathbf{q} and integrate on Ω . Then, identity (73) gives

$$\frac{1}{2} \left(\|\mathbf{q}\| + \int_{\Omega} \nabla \cdot (\mathbf{A}(\mathbf{q} \otimes \mathbf{q})) dx \right) = 0.$$

The proof is concluded applying the divergence theorem.

The numerical method becomes: find $\mathbf{u}_h = \mathbf{u}_h(\mathbf{x}, t) \in \mathcal{U}_h^N$, satisfying

$$\int_{\Omega} \partial_t \mathbf{u}_h \cdot \boldsymbol{\phi}_h dx + \int_{\Omega} (\mathbf{A} : \nabla \tilde{\mathbf{w}}_h) \cdot \boldsymbol{\phi}_h dx = 0, \quad \forall \boldsymbol{\phi}_h \in \mathcal{U}_h^N. \quad (75)$$

As in Section 4.4, we assume that $\mathbf{\Pi}_h$ and π_h are L^2 projections on \mathcal{W}_h^{N+1} and \mathcal{U}_h^N respectively. Then, Lemma 1 implies that $\tilde{\mathbf{w}}_h = \mathbf{\Pi}_h \mathbf{u}_h$ satisfies

$$\int_{\Omega} \partial_t \tilde{\mathbf{w}}_h \cdot \boldsymbol{\psi}_h dx + \int_{\Omega} (\mathbf{A} : \nabla \tilde{\mathbf{w}}_h) \cdot \boldsymbol{\psi}_h dx = 0, \quad \forall \boldsymbol{\psi}_h \in \mathcal{W}_h^{N+1}, \quad (76)$$

subject to the initial condition $\tilde{\mathbf{w}}_h(0) = \mathbf{\Pi}_h \mathbf{u}_h(0)$. As a consequence, we readily obtain energy conservation and error estimates for $\tilde{\mathbf{w}}_h$.

Lemma 3 (Discrete energy conservation) *Assume periodic or vanishing boundary conditions. Let \mathbf{u}_h be the solution of (75). Then $\tilde{\mathbf{w}}_h = \mathbf{\Pi}_h \mathbf{u}_h$ satisfies the energy conservation*

$$\frac{1}{2} \partial_t \|\tilde{\mathbf{w}}_h\|^2 = 0. \quad (77)$$

Proof Take $\boldsymbol{\psi}_h = \tilde{\mathbf{w}}_h$ in (76). Then, the proof proceeds as the one of Lemma 2.

We continue now with the error analysis of the scheme, assuming that the mesh is quasi-uniform. Let $\mathbf{H}^s(\Omega)$ be the standard vector-valued Sobolev space of $\mathbf{L}^2(\Omega)$ functions with derivatives up to order s in $\mathbf{L}^2(\Omega)$, equipped with norm and seminorm $\|\cdot\|_{\mathbf{H}^s(\Omega)}$ and $|\cdot|_{\mathbf{H}^s(\Omega)}$, see e.g. [54, Proposition 2.9].

Lemma 4 *Let $\mathbf{q} \in L^\infty(0, T; \mathbf{H}^{N+2}(\Omega))$ be the exact solution of (1) with $\mathbf{f}(\mathbf{q}) = \mathbf{A}\mathbf{q}$ and \mathbf{A} constant. Assume that the initial data satisfies $\|\mathbf{u}_h(0) - \mathbf{q}(0)\| \lesssim h^{N+1} |\mathbf{q}(0)|_{\mathbf{H}^{N+1}(\Omega)}$ and that both $\tilde{\mathbf{w}}_h$ and \mathbf{q} vanish on the boundary. Then, the solution $\tilde{\mathbf{w}}_h$ to (71) satisfies the error estimate*

$$\|\tilde{\mathbf{w}}_h(t) - \mathbf{q}(t)\| = \mathcal{O}(h^{N+1}).$$

Proof The proof uses standard FEM techniques, but we report it for completeness. Subtracting the weak form satisfied by the exact solution from (76) with test function $\psi_h = \mathbf{e}_h \doteq \tilde{\mathbf{w}}_h - \mathbf{\Pi}_h \mathbf{q} \in \mathcal{W}_h^{N+1}$, we obtain the error equation:

$$\int_{\Omega} \partial_t \mathbf{e}_h \cdot \mathbf{e}_h \, d\mathbf{x} + \int_{\Omega} (\mathbf{A} : \nabla \mathbf{e}_h) \cdot \mathbf{e}_h \, d\mathbf{x} = \int_{\Omega} (\partial_t \mathbf{q} - \partial_t \mathbf{\Pi}_h \mathbf{q}) \cdot \mathbf{e}_h \, d\mathbf{x} + \int_{\Omega} (\mathbf{A} : \nabla (\mathbf{q} - \mathbf{\Pi}_h \mathbf{q})) \cdot \mathbf{e}_h \, d\mathbf{x}.$$

Observing that $\int_{\Omega} \partial_t \mathbf{e}_h \cdot \mathbf{e}_h \, d\mathbf{x} = \frac{1}{2} \frac{d}{dt} \|\mathbf{e}_h\|^2$ and that (73) implies $\int_{\Omega} (\mathbf{A} : \nabla \mathbf{e}_h) \cdot \mathbf{e}_h \, d\mathbf{x} = 0$, we analyze the right-hand side.

The first term on the right-hand side vanishes due to the L^2 -orthogonality of $\mathbf{\Pi}_h$:

$$\int_{\Omega} (\partial_t \mathbf{q} - \partial_t \mathbf{\Pi}_h \mathbf{q}) \cdot \mathbf{e}_h \, d\mathbf{x} = \int_{\Omega} (\partial_t \mathbf{q} - \mathbf{\Pi}_h(\partial_t \mathbf{q})) \cdot \mathbf{e}_h \, d\mathbf{x} = 0.$$

For the second term, we employ the Hölder inequality and standard approximation estimates:

$$\begin{aligned} \int_{\Omega} \mathbf{A} \cdot \nabla (\mathbf{q} - \mathbf{\Pi}_h \mathbf{q}) \cdot \mathbf{e}_h \, d\mathbf{x} &\leq |\mathbf{A}|_{\infty} \|\nabla (\mathbf{q} - \mathbf{\Pi}_h \mathbf{q})\| \|\mathbf{e}_h\| \\ &\lesssim h^{N+1} |\mathbf{q}|_{\mathbf{H}^{N+2}(\Omega)} \|\mathbf{e}_h\|. \end{aligned}$$

Substituting this into the error equation and using Young's inequality yields the differential inequality:

$$\frac{d}{dt} \|\mathbf{e}_h(t)\|^2 \leq \|\mathbf{e}_h(t)\|^2 + Ch^{2(N+1)} |\mathbf{q}(t)|_{\mathbf{H}^{N+2}(\Omega)}^2.$$

We integrate from 0 to t , obtaining

$$\begin{aligned} \|\mathbf{e}_h(t)\|^2 &\leq \|\mathbf{e}_h(0)\|^2 + Ch^{2(N+1)} \int_0^t |\mathbf{q}(s)|_{\mathbf{H}^{N+2}(\Omega)}^2 \, ds + \int_0^t \|\mathbf{e}_h(s)\|^2 \, ds \\ &\leq Ch^{2(N+1)} \left(|\mathbf{q}(0)|_{\mathbf{H}^{N+1}(\Omega)}^2 + \int_0^t |\mathbf{q}(s)|_{\mathbf{H}^{N+2}(\Omega)}^2 \, ds \right) + \int_0^t \|\mathbf{e}_h(s)\|^2 \, ds \\ &=: Ch^{2(N+1)} \alpha(t) + \int_0^t \|\mathbf{e}_h(s)\|^2 \, ds. \end{aligned}$$

We have used

$$\begin{aligned} \|\mathbf{e}_h(0)\| &= \|\tilde{\mathbf{w}}_h(0) - \mathbf{\Pi}_h \mathbf{q}(0)\| \\ &= \|\mathbf{\Pi}_h(\mathbf{u}_h(0) - \mathbf{q}(0))\| \\ &\leq \|\pi_h \mathbf{q}(0) - \mathbf{q}(0)\| \\ &\lesssim h^{N+1} |\mathbf{q}(0)|_{\mathbf{H}^{N+1}(\Omega)}. \end{aligned}$$

We can now apply Grönwall's lemma in integral form and obtain

$$\begin{aligned} \|\mathbf{e}_h(t)\|^2 &\lesssim h^{2(N+1)} \left[\alpha(t) + \int_0^t \alpha(s) e^{t-s} \, ds \right] \\ &\lesssim h^{2(N+1)} \alpha(t) (e^t - 1). \end{aligned} \tag{78}$$

Finally, the triangle inequality $\|\tilde{\mathbf{w}}_h - \mathbf{q}\| \leq \|\mathbf{e}_h\| + \|\mathbf{\Pi}_h \mathbf{q} - \mathbf{q}\|$ gives the result.

Theorem 3 Let $\mathbf{q} \in L^\infty(0, T; \mathbf{H}^{N+2}(\Omega))$ be the exact solution. Then, the semi-discrete solution \mathbf{u}_h to (75) with satisfies the error estimate:

$$\|\mathbf{u}_h(t) - \mathbf{q}(t)\| = O(h^N).$$

Proof We proceed via the triangle inequality using the projected variable $\tilde{\mathbf{w}}_h = \mathbf{\Pi}_h \mathbf{u}_h$:

$$\|\mathbf{u}_h(t) - \mathbf{q}(t)\| \leq \|\mathbf{u}_h(t) - \tilde{\mathbf{w}}_h(t)\| + \|\tilde{\mathbf{w}}_h(t) - \mathbf{q}(t)\|. \quad (79)$$

The second term is bounded by Lemma 4 as:

$$\|\tilde{\mathbf{w}}_h(t) - \mathbf{q}(t)\| = O(h^{N+1}). \quad (80)$$

Then we need only to bound the first term. We define the projection offset $\delta_h(t) \doteq \mathbf{u}_h(t) - \tilde{\mathbf{w}}_h(t)$. Differentiating with respect to time and utilizing the discrete evolution equation $\partial_t \mathbf{u}_h = -\mathbf{A} : \nabla \tilde{\mathbf{w}}_h$ (which holds in \mathcal{U}_h^N since \mathbf{A} is constant and $\nabla \tilde{\mathbf{w}}_h \in \mathcal{U}_h^N$), we obtain:

$$\partial_t \delta_h = \partial_t \mathbf{u}_h - \mathbf{\Pi}_h(\partial_t \mathbf{u}_h) = (I - \mathbf{\Pi}_h) \partial_t \mathbf{u}_h = -(I - \mathbf{\Pi}_h)(\mathbf{A} : \nabla \tilde{\mathbf{w}}_h). \quad (81)$$

We multiply (81) by δ_h and we integrate on Ω obtaining:

$$\begin{aligned} \frac{1}{2} \partial_t \|\delta_h\|^2 &= - \int_{\Omega} (I - \mathbf{\Pi}_h)(\mathbf{A} : \nabla \tilde{\mathbf{w}}_h) \cdot \delta_h \, dx \\ &\leq \frac{1}{2} \|(I - \mathbf{\Pi}_h) \mathbf{A} : \nabla \tilde{\mathbf{w}}_h\|^2 + \frac{1}{2} \|\delta_h\|^2. \end{aligned}$$

To bound the first term, we introduce the gradient of the exact solution $\nabla \mathbf{q}$:

$$\begin{aligned} \|(I - \mathbf{\Pi}_h) \mathbf{A} : \nabla \tilde{\mathbf{w}}_h\| &\leq \|(I - \mathbf{\Pi}_h) \mathbf{A} : (\nabla \tilde{\mathbf{w}}_h - \nabla \mathbf{q})\| + \|(I - \mathbf{\Pi}_h) \mathbf{A} : \nabla \mathbf{q}\| \\ &\leq \|\mathbf{A} : (\nabla \tilde{\mathbf{w}}_h - \nabla \mathbf{q})\| + \|(I - \mathbf{\Pi}_h) \mathbf{A} : \nabla \mathbf{q}\| \\ &\leq |\mathbf{A}|_\infty \|\nabla \tilde{\mathbf{w}}_h - \nabla \mathbf{q}\| + \|(I - \mathbf{\Pi}_h) \mathbf{A} : \nabla \mathbf{q}\| \\ &\leq |\mathbf{A}|_\infty \|\nabla \mathbf{e}_h\| + |\mathbf{A}|_\infty \|\nabla(\mathbf{I} - \mathbf{\Pi}_h) \mathbf{q}\| + \|(I - \mathbf{\Pi}_h) \mathbf{A} : \nabla \mathbf{q}\|. \end{aligned}$$

We bound the first term using an inverse inequality and (78):

$$|\mathbf{A}|_\infty \|\nabla \mathbf{e}_h\| \lesssim h^{-1} \|\mathbf{e}_h\| \lesssim h^N \sqrt{\alpha(t)(e^t - 1)}.$$

The second and third terms can be bounded with standard approximation properties of $\mathbf{\Pi}_h$:

$$|\mathbf{A}|_\infty \|\nabla(\mathbf{I} - \mathbf{\Pi}_h) \mathbf{q}\| + \|(I - \mathbf{\Pi}_h) \mathbf{A} : \nabla \mathbf{q}\| \lesssim h^N |\mathbf{q}|_{\mathbf{H}^{N+1}(\Omega)}.$$

Combining these two estimates, we obtain:

$$\frac{1}{2} \partial_t \|\delta_h(t)\|^2 \leq O(h^{2N}) + \frac{1}{2} \|\delta_h(t)\|^2.$$

Integrating from 0 to t :

$$\|\delta_h(t)\|^2 \leq \|\delta_h(0)\|^2 + O(h^{2N}) + \int_0^t \|\delta_h(s)\|^2 \, ds$$

$$\leq O(h^{2N}) + \int_0^t \|\delta_h(s)\|^2 ds.$$

We have used the following bound on the initial offset:

$$\|\delta_h(0)\| = \|(I - \mathbf{\Pi}_h)\mathbf{u}_h(0)\| \leq \|\mathbf{u}_h(0) - \mathbf{q}(0)\| + \|(I - \mathbf{\Pi}_h)\mathbf{q}(0)\| \lesssim h^{N+1}|\mathbf{q}(0)|_{\mathbf{H}^{N+1}}.$$

Then the proof is concluded applying Grönwall's lemma.

5 More efficient flux reconstruction(s)

In order to make the global L^2 projection more efficient, we propose the following simple strategy to find a suitable *initial guess* for the conjugate gradient method that is used to solve (6). The approach is based on a quasi-interpolation procedure, similar to that introduced by Ern and Guermond in [53]. For each element T_k define a reconstruction stencil \mathcal{S}_k which contains all the elements that share a common vertex with T_k . Then solve the following *local* L^2 problem exactly,

$$\int_{\mathcal{S}_k} \psi_i \psi_j d\mathbf{x} \tilde{\mathbf{w}}_j^k(t) = \int_{\mathcal{S}_k} \psi_i \phi_j d\mathbf{x} \hat{\mathbf{u}}_j(t), \quad (82)$$

which is easy to solve, since the dimension of the stencil mass matrix to be inverted is now sufficiently small and does not depend on the total number of elements $|\mathcal{T}_h|$ in \mathcal{T}_h , but only on the number of elements $|\mathcal{S}_k|$ in the reconstruction stencil \mathcal{S}_k . The inverse of this localized FEM mass matrix can actually be precomputed for each T_k , multiplied with the right hand side matrix and stored for each element. Note that in (82) the degrees of freedom $\tilde{\mathbf{w}}_j^k(t)$ are computed individually for each element T_k and therefore global continuity is *not* yet established. We then compute the *initial guess* for the degrees of freedom of the globally continuous representation $\tilde{\mathbf{w}}_h$ as

$$\tilde{\mathbf{w}}_j^0(t) = \frac{1}{|\mathcal{N}_j|} \sum_{T_k \in \mathcal{N}_j} \tilde{\mathbf{w}}_j^k(t), \quad (83)$$

where \mathcal{N}_j is the set of triangles T_k that contain node number j . For internal degrees of freedom, i.e. those inside T_k one clearly has $|\mathcal{N}_j| = 1$, for nodes in the interior of edges (2D) / faces (3D) one has $|\mathcal{N}_j| = 2$, and for elements in the interior of edges (3D) or on vertices (both 3D and 2D) one has in general a much larger number of elements, corresponding to those elements that share a common edge (3D) or vertex (3D and 2D). With the initial guess (83) one then solves the full problem (6) via the matrix-free conjugate gradient method up to a desired tolerance.

5.1 Genuinely multi-dimensional upwinding via the N-scheme

The idea outlined here is a local alternative to the L^2 projection and is based on the ideas of the N -scheme of residual distribution (RD) methods [1, 87, 89, 90, 97] and has

recently also been used in semi-discrete active flux (AF) / PAMPA schemes [2, 3, 6, 7]. We evaluate $\hat{\mathbf{w}}$ from $\hat{\mathbf{u}}$ by

$$\hat{\mathbf{w}}_j(t) = \mathbf{N}_j^{-1} \sum_{T_k \in \mathcal{N}_j} \mathbf{K}_{k,j}^+ \tilde{\mathbf{w}}_j^k(t), \quad (84)$$

with

$$\mathbf{N}_j = \sum_{T_k \in \mathcal{N}_j} \mathbf{K}_{k,j}^+ \quad (85)$$

and

$$\mathbf{K}_{k,j}^+ = \mathbf{R}_n (\max(\Lambda_n, 0) + \varepsilon \mathbf{I}) \mathbf{R}_n^{-1} \quad (86)$$

with \mathbf{R}_n and Λ_n , the matrix of right eigenvectors and the diagonal matrix of eigenvalues of the Jacobian matrix

$$\mathbf{A}_n = \frac{\partial(\mathbf{f} \cdot \mathbf{n}_{k,j})}{\partial \mathbf{q}}$$

of the hyperbolic system (1) in normal direction $\mathbf{n}_{k,j}$, which is the outward-pointing normal vector for degree of freedom j in element k . The term $\varepsilon \mathbf{I}$ is here to avoid any singularity of \mathbf{N}_j . This kind of singularity may occur in cases where the flow is aligned with one of the faces. In practice we take a small number of the order of 10^{-12} or simply half of the volume of the element. For internal degrees of freedom we simply set $\mathbf{K}_{k,j}^+ = \mathbf{I}$ with \mathbf{I} the identity matrix. Of course there $\varepsilon = 0$. For degrees of freedom in the vertices of an element we use the corner normal [1, 3, 6, 7, 21, 32, 42, 70, 77, 78, 87, 91], for degrees of freedom internal of an edge/face we use the edge/face normal. In the future we will also consider the use of composite finite volume schemes [18, 24, 63] for the calculation of numerical fluxes in all degrees of freedom of the finite element space \mathcal{W}_h^{N+1} , which can be either internal, or on faces, on edges or on vertices.

6 Numerical results

In the following we show numerical results obtained with the new CG-DG scheme applied to three different linear and nonlinear hyperbolic PDE systems, namely the equations of linear acoustics, the vacuum Maxwell equations and the nonlinear compressible Euler equations.

6.1 Equations of linear acoustics

The equations of linear acoustics read

$$\frac{\partial \rho \mathbf{v}}{\partial t} + \nabla p = 0, \quad (87)$$

$$\frac{\partial p}{\partial t} + \rho c^2 \nabla \cdot \mathbf{v} = 0, \quad (88)$$

with constant fluid density ρ , velocity vector \mathbf{v} , pressure p and constant sound speed c . The above system satisfies the following extra conservation law for the total energy density $\mathcal{E} = \frac{1}{2}\rho\mathbf{v}^2 + \frac{1}{2\rho c^2}p^2$:

$$\frac{\partial \mathcal{E}}{\partial t} + \nabla \cdot (\mathbf{v}p) = 0. \quad (89)$$

From the momentum equation (87) it is obvious that the velocity field remains curl-free if it was so initially, i.e. the following involution holds

$$\nabla \times \mathbf{v} = 0. \quad (90)$$

This means that in the new CG-DG scheme introduced in this paper, the discrete velocity field $\mathbf{v}_h \in \mathcal{U}_h^N$ must be initialized as the discrete gradient of a scalar potential $Z_h \in \mathcal{W}_h^{N+1}$ so that (90) holds at the discrete level. In the presence of discontinuities and in order to keep the velocity field curl-free, the artificial viscosity is chosen such that its structure is compatible with the equations. Following [93], the pressure and the velocity fields used in the numerical flux field are modified as follows:

$$\tilde{\mathbf{v}}_h = \mathbf{v}(\tilde{\mathbf{w}}_h) - \epsilon \tilde{\nabla} p_h, \quad \tilde{p}_h = p(\tilde{\mathbf{w}}_h) - \epsilon \tilde{\nabla} \cdot \mathbf{v}_h, \quad (91)$$

with $\mathbf{v}(\tilde{\mathbf{w}}_h)$ and $p(\tilde{\mathbf{w}}_h)$ the averaged states given by $\tilde{\mathbf{w}}_h$ and ϵ the artificial viscosity coefficient given already above.

6.1.1 Smooth acoustic wave propagation

The first test for linear acoustics is taken from [5], with initial condition

$$\mathbf{v}(\mathbf{x}, 0) = 0, \quad p(\mathbf{x}, 0) = p_0 \exp\left(-\frac{1}{2}\mathbf{x}^2/\sigma^2\right) \quad (92)$$

and $p_0 = 1$ and $\sigma = 0.05$. Simulations are carried out in the domain $\Omega = [-\frac{1}{2}, +\frac{1}{2}]^d$ until a final time of $t = 10$, without any artificial viscosity. We use an unstructured triangular mesh composed of a total number of 2028 triangles with $N_x = N_y = 30$ elements along each edge of the computational domain. We use a CG-DG scheme of polynomial approximation degree $N = 3$. The computational results obtained are depicted in Figure 3. As expected, the method conserves total energy up to machine precision even over long times and the discrete velocity field remains curl-free up to machine precision, as expected. The linear growth in the curl error is due to the accumulation of roundoff errors in the computer. The growth of the total energy conservation error is due to the time discretization which is not exactly energy conservative and our results hold only at the semi-discrete level so far. For this reason, future research will also concern the use of exactly energy conservative time integrators.

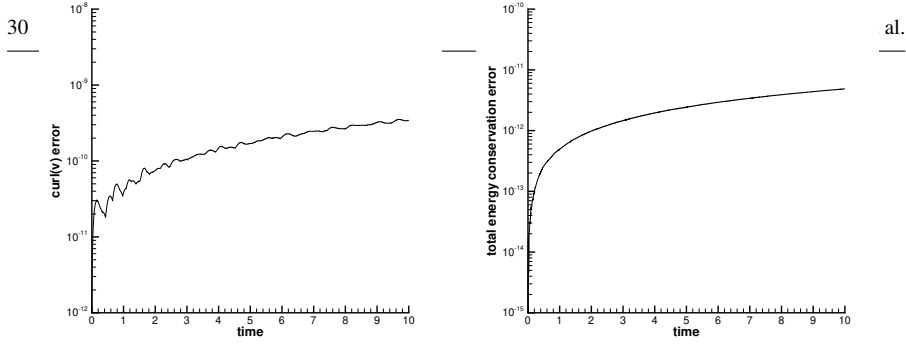


Fig. 3 Smooth acoustic wave propagation. Time evolution of the L^∞ error of the curl of the velocity field (left) and time evolution of the total energy conservation error (right).

6.1.2 Acoustic waves with discontinuities

Next, we consider a test problem that contains a nontrivial initial velocity field and an initially discontinuous pressure profile. The initial velocity is computed as the gradient of a scalar potential Z and reads

$$\mathbf{v}(\mathbf{x}, 0) = \nabla Z, \quad \text{with} \quad Z = \sin(2\pi x) \sin(2\pi y), \quad (93)$$

while the initial pressure is

$$p(\mathbf{x}, 0) = \begin{cases} 1 & \text{if } r \leq R, \\ 0 & \text{if } r > R, \end{cases} \quad (94)$$

with $r = \|\mathbf{x}\|$ and $R = 0.25$. The computational domain is $\Omega = [-\frac{1}{2}, +\frac{1}{2}]^2$ with periodic boundaries everywhere. The unstructured mesh is composed of 3608 triangles, with 40 elements along each edge of the square domain. Simulations are carried out until $t = 0.1$ with the new CG-DG scheme with polynomial approximation degree $N = 3$ and the compatible artificial viscosity activated, since the solution presents discontinuities. The computational results are depicted in Figures 4 and 5. One can observe that the curl errors remain of the order of machine precision, despite a linear growth that is due to the accumulation of roundoff errors in the computer. The energy is decreasing since the method is dissipative due to the presence of the artificial viscosity.

6.2 Vacuum Maxwell equations

The vacuum Maxwell equations with unit light speed and in the absence of charges are

$$\frac{\partial \mathbf{B}}{\partial t} + \nabla \times \mathbf{E} = 0, \quad (95)$$

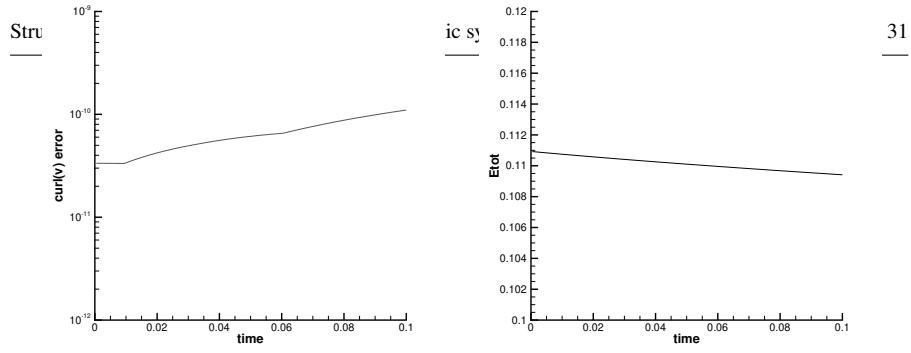


Fig. 4 Acoustic waves with discontinuities. Time evolution of the L^∞ error of the curl of the velocity field (left) and time evolution of the total energy (right). The method is dissipative since the artificial viscosity for the treatment of discontinuities is switched on.

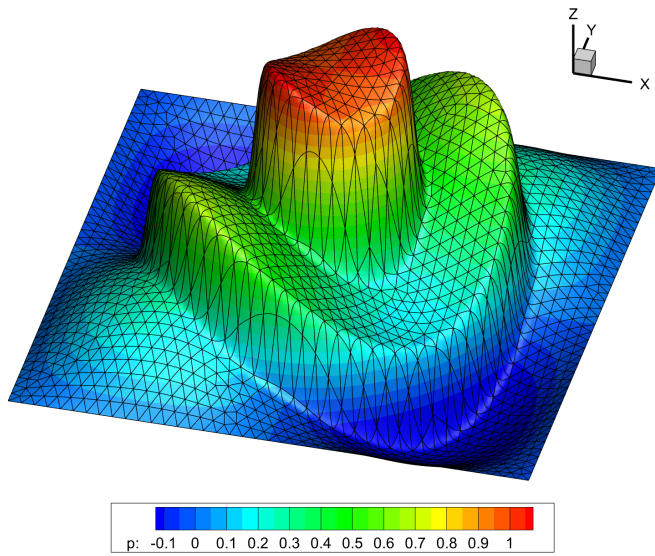


Fig. 5 3D plot of the pressure and the computational mesh at time $t = 0.1$.

$$\frac{\partial \mathbf{E}}{\partial t} - \nabla \times \mathbf{B} = 0. \quad (96)$$

Here, \mathbf{E} and \mathbf{B} are the electric and magnetic field, respectively. The system satisfies the following extra conservation law for the total energy density $\mathcal{E} = \frac{1}{2}\mathbf{E}^2 + \frac{1}{2}\mathbf{B}^2$:

$$\frac{\partial \mathcal{E}}{\partial t} + \nabla \cdot (\mathbf{E} \times \mathbf{B}) = 0. \quad (97)$$

From the Maxwell equations (95) and (96) it becomes immediately clear that both, the magnetic field as well as the electric field must remain divergence-free for all times, if they were initially divergence-free. This means that the following two involutions must hold:

$$\nabla \cdot \mathbf{B} = 0, \quad \text{and} \quad \nabla \cdot \mathbf{E} = 0. \quad (98)$$

Hence, for the CG-DG scheme the initial electric and magnetic fields in \mathcal{U}_h^N must be computed as the discrete curl of two vector potentials in \mathcal{W}_h^{N+1} in order to have (98) satisfied at the discrete level for all times. In order to treat solutions with discontinuities and to maintain at the same time the divergence-free property of the magnetic and the electric field, the artificial viscosity must have a structure that is compatible with the equations. Therefore, the electric and magnetic fields used in the fluxes are modified as follows:

$$\tilde{\mathbf{E}}_h = \mathbf{E}(\tilde{\mathbf{w}}_h) + \epsilon \tilde{\nabla} \times \mathbf{B}_h, \quad \tilde{\mathbf{B}}_h = \mathbf{B}(\tilde{\mathbf{w}}_h) - \epsilon \tilde{\nabla} \times \mathbf{E}_h. \quad (99)$$

with $\mathbf{E}(\tilde{\mathbf{w}}_h)$ and $\mathbf{B}(\tilde{\mathbf{w}}_h)$ the electric and magnetic fields contained in $\tilde{\mathbf{w}}_h$ and ϵ the artificial viscosity coefficient.

6.2.1 Smooth electromagnetic wave propagation

To test the properties of our new CG-DG scheme, we solve the following test problem with initial condition data

$$\mathbf{B}(\mathbf{x}, 0) = \mathbf{B}_0 \exp\left(-\frac{1}{2}\mathbf{x}^2/\sigma^2\right), \quad \mathbf{E}(\mathbf{x}, 0) = \mathbf{E}_0 \exp\left(-\frac{1}{2}\mathbf{x}^2/\sigma^2\right). \quad (100)$$

Simulations are run in the domain $\Omega = [-\frac{1}{2}, +\frac{1}{2}]^2$ until a final time of $t = 10$, using a polynomial approximation degree of $N = 3$. The mesh contains 2028 triangles with $N_x = N_y = 30$ elements along each edge of the computational domain. For the initial data we set $\mathbf{B}_0 = 0$ and $\mathbf{E}_0 = (0, 0, 1)$. The half width is chosen as $\sigma = 0.05$. The computational results are shown in Figure 6. As expected, the method conserves total energy and the magnetic and electric field remain both divergence-free up to machine precision. The linear growth in time in the divergence errors is due to the accumulation of roundoff errors in the computer, while the linear growth in time of the total energy conservation error is due to time discretization errors as our energy conservation property only holds on the semi-discrete level.

6.2.2 Electromagnetic waves with discontinuities

We consider the following test problem with nontrivial initial magnetic and electric field, including discontinuities. The x and y components of the initial electric and magnetic field are computed as the curl of a vector potential \mathbf{A} :

$$\mathbf{B}(\mathbf{x}, 0) = \nabla \times \mathbf{A}, \quad \mathbf{E}(\mathbf{x}, 0) = \nabla \times \mathbf{A}, \quad \text{with} \quad \mathbf{A} = (0, 0, \sin(2\pi x) \sin(2\pi y)), \quad (101)$$

while the initial z component of the electric and magnetic field are initialized by

$$E_3(\mathbf{x}, 0), B_3(\mathbf{x}, 0) = \begin{cases} 1 & \text{if } r \leq R, \\ 0 & \text{if } r > R, \end{cases} \quad (102)$$

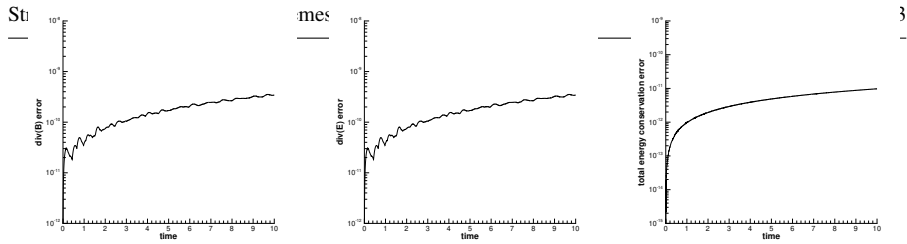


Fig. 6 Smooth electromagnetic wave propagation. Time evolution of the L^∞ error of the divergence of the magnetic field (left), of the divergence of the electric field (center) and time evolution of the total energy conservation error (right).

with $r = \|\mathbf{x}\|$ and $R = 0.25$. The computational domain is $\Omega = [-\frac{1}{2}, +\frac{1}{2}]^2$ with periodic boundaries everywhere. The unstructured mesh is composed of 3608 triangles, with 40 elements along each edge of the square domain. Simulations are carried out until $t = 0.1$ with the new CG-DG scheme with polynomial approximation degree $N = 3$ and the compatible artificial viscosity activated. The computational results are depicted in Figures 7 and 8. The divergence errors of both the magnetic and the electric field remain of the order of machine precision, as expected. The observable linear growth in the errors is due to the accumulation of roundoff errors in the computer. In this test the energy is decreasing, since the method is dissipative due to the presence of the artificial viscosity.

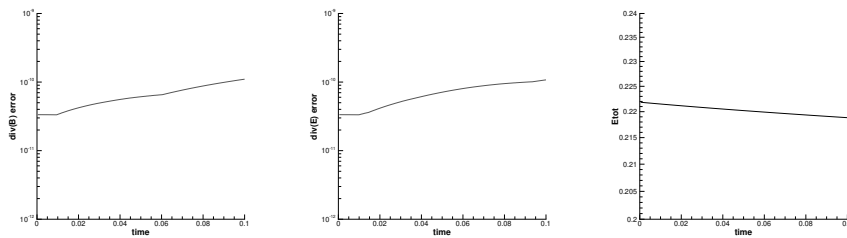


Fig. 7 Electromagnetic waves with discontinuities. Time evolution of the L^∞ errors of the divergence of the magnetic field (left) and of the divergence of the electric field (center) as well as the time evolution of the total energy (right). The method is dissipative since the artificial viscosity for the treatment of discontinuities is switched on.

6.3 Nonlinear compressible Euler equations

So far all PDE systems considered in this section were linear and did not present shock waves. Here we apply our new CG-DG scheme also to a nonlinear system of

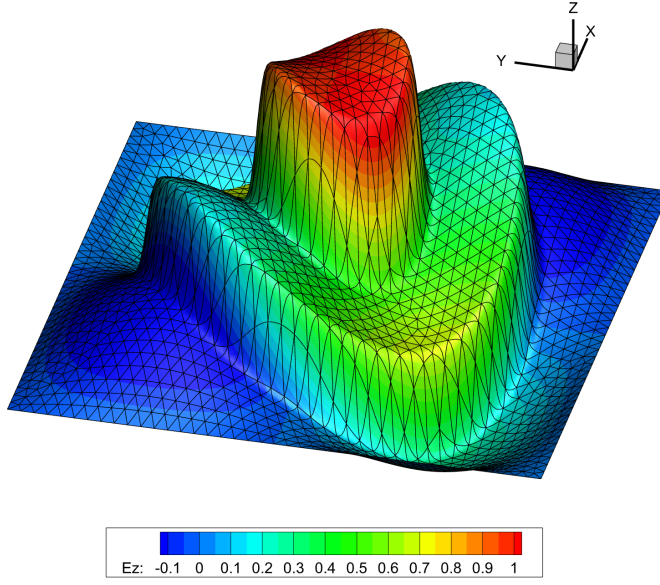


Fig. 8 3D plot of the z component of the magnetic field, coloured by the z component of the electric field, together with the computational mesh at time $t = 0.1$.

conservation laws, namely the compressible Euler equations. They read

$$\frac{\partial \rho}{\partial t} + \nabla \cdot (\rho \mathbf{v}) = 0, \quad (103)$$

$$\frac{\partial(\rho \mathbf{v})}{\partial t} + \nabla \cdot (\rho \mathbf{v} \otimes \mathbf{v}) + \nabla p = 0, \quad (104)$$

$$\frac{\partial \mathcal{E}}{\partial t} + \nabla \cdot (\mathbf{v}(\mathcal{E} + p)) = 0, \quad (105)$$

with ρ the fluid density, \mathbf{v} the velocity vector, p the pressure, $\mathcal{E} = \rho E = \frac{1}{2}\rho \mathbf{v}^2 + \rho e$ the total energy density and e the specific internal energy. For ideal gases the internal energy density ρe is given by the following equation of state:

$$\rho e = \frac{p}{\gamma - 1}, \quad (106)$$

with $\gamma = c_p/c_v$ the ratio of specific heats, where c_p is the specific heat at constant pressure and c_v is the specific heat at constant volume. For diatomic gases it typically assumes the value $\gamma = 1.4$. The Euler equations satisfy the following entropy inequality

$$\frac{\partial(\rho S)}{\partial t} + \nabla \cdot (\mathbf{v}\rho S) \geq 0, \quad (107)$$

with the specific entropy S that is linked to the other state variables again via the equation of state

$$e = \frac{\rho^{\gamma-1}}{\gamma - 1} \exp(S/c_v). \quad (108)$$

However, in this paper the entropy inequality is not explicitly considered at the discrete level. Constructing a provably entropy stable version of our new CG-DG scheme is the topic of future research and out of scope of this work. However, some basic ideas on how to achieve this in the special case $N = 0$ have been outlined in Section 3.

6.4 Numerical convergence study for the isentropic vortex

The order of accuracy of the new CG-DG scheme is experimentally verified via the well-known isentropic vortex problem, see [64]. The problem is solved in a periodic domain $\Omega = [0, 10]^2$ until a final time of $t = 0.2$. In this isentropic flow the entropy is constant. The velocity, temperature, density and pressure profiles read

$$\mathbf{v} = \frac{\varepsilon}{2\pi} e^{\frac{1-r^2}{2}} \begin{pmatrix} 5-y \\ x-5 \end{pmatrix}, \quad \rho = 1 + (1 + \delta T)^{\frac{1}{\gamma-1}}, \quad p = 1 + (1 + \delta T)^{\frac{\gamma}{\gamma-1}}$$

with the temperature fluctuation

$$\delta T = -\frac{(\gamma-1)\varepsilon^2}{8\gamma\pi^2} e^{1-r^2}, \quad (109)$$

$r^2 = (x-5)^2 + (y-5)^2$ and $\varepsilon = 5$. The above vortex is a stationary solution of the compressible Euler equations, hence $\mathbf{q}(\mathbf{x}, t) = \mathbf{q}(\mathbf{x}, 0)$. The numerical convergence study of the CG-DG schemes is carried out with different polynomial approximation degrees N on a sequence of successively refined unstructured triangular meshes composed of $N_x \times N_y$ elements on the boundaries of Ω . In Tables 1 and 2 we report the L^2 error norms computed for the DG solution $\mathbf{u}_h \in \mathcal{U}_h^N$ and for the CG solution $\tilde{\mathbf{w}}_h \in \mathcal{W}_h^{N+1}$, respectively, at the final time, together with the numerical convergence rates of the scheme. Results are shown for the density ρ , the momentum density component ρv_1 and the energy density \mathcal{E} .

6.5 2D circular Sod problem

As last test case we consider a circular version of the Sod problem. The computational domain is $\Omega = [-0.5; +0.5]^2$ and the initial condition is given by

$$\mathbf{q}(\mathbf{x}, 0) = \begin{cases} \mathbf{q}_L & \text{if } r \leq R \\ \mathbf{q}_R & \text{if } r > R, \end{cases} \quad (110)$$

with \mathbf{q}_L and \mathbf{q}_R the inner and outer states, respectively, and $r = \sqrt{x^2 + y^2}$ being the radial coordinate. The initial discontinuity is placed at a radius of $R = 0.25$. For the inner state we set the density and the pressure to $\rho_L = 1$ and $p_L = 1$, while in the outer state we impose $\rho_R = 0.125$ and $p_R = 0.1$. The initial velocity is set to zero everywhere and the final time is $t = 0.1$. We solve the problem with the new CG-DG scheme with polynomial approximation degree of $N = 3$ using a very coarse unstructured triangular mesh of characteristic mesh spacing $h = 1/40$ leading to a

Table 1 L^2 error norms and numerical convergence results for the DG approximation $\mathbf{u}_h \in \mathcal{U}_h^N$ of density ρ , momentum density ρv_1 and total energy density \mathcal{E} at time $t = 0.2$ obtained with the CG-DG scheme applied to the isentropic vortex of the compressible Euler equations.

N_x	ρ	ρv_1	\mathcal{E}	$\mathcal{O}(\rho)$	$\mathcal{O}(\rho v_1)$	$\mathcal{O}(\mathcal{E})$
CG-DG scheme - $N = 0$ - errors for the DG solution $\mathbf{u}_h \in \mathcal{U}_h^N$						
40	1.67642E-01	2.29380E-01	5.81673E-01			
60	1.21994E-01	1.72001E-01	4.27463E-01	0.78	0.71	0.76
80	9.25884E-02	1.29276E-01	3.22676E-01	0.96	0.99	0.98
100	8.80546E-02	1.08306E-01	3.11585E-01	0.22	0.79	0.16
120	7.36997E-02	9.52808E-02	2.60744E-01	0.98	0.70	0.98
CG-DG scheme - $N = 1$ - errors for the DG solution $\mathbf{u}_h \in \mathcal{U}_h^N$						
20	5.27050E-02	6.76255E-02	1.89896E-01			
40	2.38234E-02	2.29451E-02	8.30463E-02	1.15	1.56	1.19
60	1.50982E-02	1.31298E-02	5.25043E-02	1.12	1.38	1.13
80	1.11210E-02	9.52188E-03	3.84636E-02	1.06	1.12	1.08
100	9.10958E-03	7.26372E-03	3.16733E-02	0.89	1.21	0.87
CG-DG scheme - $N = 2$ - errors for the DG solution $\mathbf{u}_h \in \mathcal{U}_h^N$						
20	5.10101E-03	5.50622E-03	1.85874E-02			
30	1.76491E-03	1.80041E-03	6.71338E-03	2.62	2.76	2.51
40	8.98201E-04	8.45640E-04	3.46203E-03	2.35	2.63	2.30
60	3.85040E-04	3.04814E-04	1.45175E-03	2.09	2.52	2.14
80	2.03809E-04	1.49610E-04	7.74628E-04	2.21	2.47	2.18
CG-DG scheme $N = 3$ - errors for the DG solution $\mathbf{u}_h \in \mathcal{U}_h^N$						
10	5.45417E-03	6.89276E-03	2.02366E-02			
20	4.93639E-04	5.56104E-04	1.92538E-03	3.47	3.63	3.39
30	1.31371E-04	1.44984E-05	5.17261E-04	3.26	3.32	3.24
40	5.33164E-05	5.85443E-05	2.12223E-04	3.13	3.15	3.10
60	1.90272E-05	1.70220E-05	7.33671E-05	2.54	3.05	2.62
CG-DG scheme $N = 4$ - errors for the DG solution $\mathbf{u}_h \in \mathcal{U}_h^N$						
8	2.51710E-03	2.99501E-03	2.02366E-02			
12	7.58331E-04	9.18014E-04	1.92538E-03	2.96	2.92	2.99
16	2.01162E-04	2.36542E-04	5.17261E-04	4.61	4.71	4.31
20	7.82146E-05	9.04805E-05	2.12223E-04	4.23	4.31	3.99
30	1.46141E-05	1.15048E-05	7.33671E-05	4.14	5.09	4.36

total number of 3608 triangles. In this test, the artificial viscosity regularization is needed and the indicator is globally set to $\chi_j = 1$. The reference solution is obtained by solving a 1D radial Euler system with source terms using a classical second-order MUSCL-Hancock scheme on a very fine mesh, as described in detail in [96]. In Fig. 9 a comparison of the reference solution with the numerical results obtained at the aid of the new CG-DG scheme on a 1D cut along the axis $y = 0$ is provided for density, radial velocity and pressure. One observes overall a good agreement. In the left panel of Fig. 10 a 3D plot of the coarse mesh used in our simulation as well as the density color contours are shown at the final time.

In order to verify the new pointwise conservation property (68) we place 4 observation points \mathbf{x}_o in the domain Ω . The observation points deliberately do *not* coincide with any mesh point or with any location of the degrees of freedom of $\tilde{\mathbf{w}}_h$. We also define 3 circular control volumes V_1 , V_2 and V_3 of radius $r_c = 0.015$ with centers

Table 2 L^2 error norms and numerical convergence results for the CG approximation $\tilde{\mathbf{w}}_h \in \mathcal{W}_h^{N+1}$ of density ρ , momentum density ρv_1 and total energy density \mathcal{E} at time $t = 0.2$ obtained with the CG-DG scheme applied to the isentropic vortex of the compressible Euler equations.

N_x	ρ	ρv_1	\mathcal{E}	$\mathcal{O}(\rho)$	$\mathcal{O}(\rho v_1)$	$\mathcal{O}(\mathcal{E})$
CG-DG scheme - $N = 0$ - errors for the CG solution $\tilde{\mathbf{w}}_h \in \mathcal{W}_h^{N+1}$						
40	9.62492E-02	1.34913E-01	3.24378E-01			
60	6.30125E-02	9.07302E-02	2.13701E-01	1.04	0.98	1.03
80	4.52909E-02	7.50398E-02	1.49074E-01	1.15	0.66	1.25
100	3.84668E-02	5.56813E-02	1.29215E-01	0.73	1.34	0.64
120	3.19719E-02	5.09359E-02	1.04345E-01	1.01	0.49	1.17
CG-DG scheme - $N = 1$ - errors for the CG solution $\tilde{\mathbf{w}}_h \in \mathcal{W}_h^{N+1}$						
20	3.30643E-02	5.72675E-02	1.22017E-01			
40	8.23815E-03	1.43129E-02	2.98509E-02	2.00	2.00	1.19
60	3.67002E-03	6.36043E-03	1.33411E-02	1.99	2.00	1.13
80	2.03138E-03	3.53558E-03	7.39153E-03	2.06	2.04	1.08
100	1.27419E-03	2.27001E-03	4.64204E-03	2.09	1.99	0.87
CG-DG scheme - $N = 2$ - errors for the CG solution $\tilde{\mathbf{w}}_h \in \mathcal{W}_h^{N+1}$						
20	2.42575E-03	3.11246E-03	6.50865E-03			
30	5.93065E-04	9.69959E-04	1.94752E-03	3.47	2.88	2.98
40	2.16405E-04	4.13384E-04	9.15284E-04	3.50	2.96	2.62
60	8.09417E-05	1.12814E-04	2.12516E-04	2.43	3.20	3.60
80	2.63649E-05	5.05651E-05	1.05949E-04	3.90	2.79	2.42
CG-DG scheme $N = 3$ - errors for the CG solution $\tilde{\mathbf{w}}_h \in \mathcal{W}_h^{N+1}$						
10	2.78313E-03	4.33882E-03	8.05779E-03			
20	1.73256E-04	2.69514E-04	5.44824E-04	4.01	4.01	3.89
30	3.11688E-05	5.47120E-05	1.24977E-04	4.23	3.93	3.63
40	9.11550E-06	1.70552E-05	3.36556E-05	4.27	4.05	4.56
60	1.80827E-06	4.77257E-06	6.33037E-06	3.99	3.14	4.12
CG-DG scheme $N = 4$ - errors for the CG solution $\tilde{\mathbf{w}}_h \in \mathcal{W}_h^{N+1}$						
8	1.36758E-03	1.66682E-03	3.83420E-03			
12	3.58710E-04	5.09206E-04	9.44364E-04	3.30	2.92	3.46
16	6.43038E-05	9.53276E-05	2.07467E-04	5.97	5.82	5.27
20	1.99842E-05	2.90708E-05	5.95100E-05	5.24	5.32	5.60
30	2.60846E-06	5.18256E-06	6.69142E-06	5.02	4.25	5.39

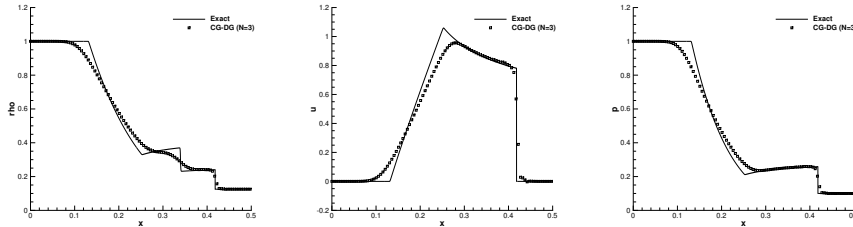


Fig. 9 Cut through the numerical solution along the axis $y = 0$ at the final time $t = 0.1$ and comparison with the reference solution for density (left), radial velocity (center) and pressure (right).

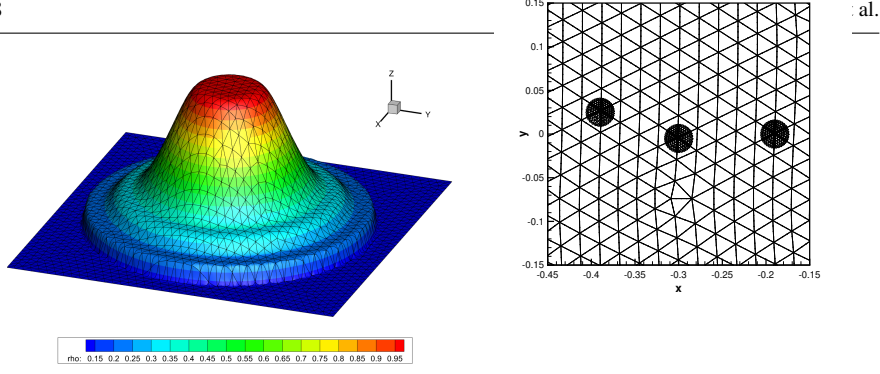


Fig. 10 2D circular Sod problem. Mesh and 3D view of the numerical solution $\tilde{\mathbf{w}}_h$ for density at $t = 0.1$ (left). Zoom into the mesh and visualization of three circular control volumes V_1 , V_2 and V_3 and their approximation via the union of curved isoparametric triangles of degree $n_c = 6$ (right).

Table 3 Locations of the control points \mathbf{x}_o used to verify (68) and centers \mathbf{x}_c of the circular control volumes V_i used to verify (70). The nearest mesh point \mathbf{x}_n is also given to show that $\mathbf{x}_o \neq \mathbf{x}_n$ and $\mathbf{x}_c \neq \mathbf{x}_n$. The L^∞ errors observed in all time steps and Runge-Kutta stages during the entire simulation are reported.

\mathbf{x}_o	\mathbf{x}_n	$L^\infty(\rho)$	$L^\infty(\rho v_1)$	$L^\infty(\rho v_2)$	$L^\infty(\rho E)$
(-3.00E-01, 0.00E+00)	(-3.011E-01, -4.029E-03)	3.475E-13	6.044E-13	2.506E-13	1.064E-12
(-2.50E-01, 0.00E+00)	(-2.569E-01, -7.774E-03)	7.394E-14	2.025E-13	7.976E-13	2.283E-13
(-2.00E-01, 0.00E+00)	(-1.901E-01, 7.435E-04)	2.394E-13	7.529E-13	3.360E-13	7.425E-13
(-1.50E-01, 0.00E+00)	(-1.463E-01, -2.619E-03)	1.554E-13	8.773E-13	2.946E-13	5.382E-13
\mathbf{x}_c	\mathbf{x}_n	$L^\infty(\rho)$	$L^\infty(\rho v_1)$	$L^\infty(\rho v_2)$	$L^\infty(\rho E)$
(-3.00E-01, -5.00E-03)	(-3.011E-01, -4.029E-03)	1.041E-11	2.131E-11	7.491E-12	5.656E-11
(-1.90E-01, 0.00E+00)	(-1.901E-01, 7.435E-04)	8.595E-13	1.077E-12	1.107E-12	3.379E-12
(-3.90E-01, 2.50E-02)	(-3.888E-01, 2.716E-02)	5.026E-10	8.298E-10	2.381E-10	2.062E-09

\mathbf{x}_c in order to check the integral form of the conservation law over generic control volumes V , see eqn. (70). The integrals appearing in the integral form (70) over arbitrary control volumes V are computed by approximating the circular control volumes via a set of isoparametric triangles of approximation degree $n_c = 6$ for the geometry and using suitable one and two-dimensional Gaussian quadrature formulas [94] in the subvolumes and on the boundary segments. We use $m_c = n_c + 2$ quadrature points in 1D and m_c^2 quadrature points in 2D. In Table 3 we report the coordinates \mathbf{x}_o and \mathbf{x}_c together with the coordinates of the nearest mesh point \mathbf{x}_n with $\mathbf{x}_o \neq \mathbf{x}_n$ and $\mathbf{x}_c \neq \mathbf{x}_n$, as well as the L^∞ errors of (68) and (70) observed for all Runge-Kutta stages and time steps during the entire simulation for all state variables \mathbf{q} . As expected, the error is of the order of machine precision, providing numerical evidence that the theoretical properties also hold in our practical implementation.

7 Conclusions

In this paper we have introduced a new class of continuous discontinuous Galerkin finite element schemes (CG-DG) for linear and nonlinear hyperbolic systems of partial differential equations on unstructured simplex meshes. The key idea of the method relies on two compatible discrete ansatz spaces: a *discontinuous one* (DG) \mathcal{U}_h^N based on piecewise polynomials of degree N that is used to discretize the *state vector* of the system, and a *globally continuous one* \mathcal{W}_h^{N+1} using piecewise polynomials of degree $N + 1$ for the representation of the *discrete flux field*. Indeed, the introduction of a globally continuous discrete flux field is a major pillar in our new method. The continuous discrete flux field is reconstructed from the discontinuous state vector represented and evolved in the DG scheme. The proposed scheme is by construction locally pointwise conservative and satisfies both vector calculus identities at the discrete level exactly pointwise everywhere. The discrete vector calculus identities are an immediate consequence of the fact that the two discrete nabla operators appearing in the CG-DG scheme satisfy a discrete Schwarz theorem.

Our approach can also be seen as a direct and natural extension of cell-centered finite volume schemes with vertex-based fluxes [20,21,32,39,42,55,77,78] to arbitrary high order of accuracy in space.

Thanks to a suitable artificial viscosity regularization, our method maintains all properties also in the presence of shock waves and discontinuities.

Future work will concern the extension to more general unstructured meshes and to a discretely thermodynamically compatible formulation for nonlinear HTC systems, see e.g. [4, 29]. We furthermore plan to extend the method to the MHD equations, the equations of nonlinear hyperelasticity in Eulerian coordinates [48, 49, 85] as well as to compressible multi-phase flows with surface tension [34], all of which contain divergence and/or curl constraints for some vector fields of the system. Since the new CG-DG scheme automatically preserves divergence and curl involutions exactly at the discrete level, it may be an interesting method to be tried in the context of numerical general relativity, in particular in the context of first order hyperbolic reductions of the Einstein field equations [46, 47, 50–52], which come along with a large number of curl involutions. We also want to investigate the use of more sophisticated and provably bound-preserving limiters, as well as energy-conserving time integrators [26, 27].

Acknowledgments

M.D. and E.Z. are members of the INdAM GNCS group. M.D. also acknowledges the financial support received from the Fondazione Caritro under the project SOPHOS and the support from the European Research Council (ERC) under the European Unions Horizon 2020 research and innovation programme, Grant agreement No. ERC-ADG-2021-101052956-BEYOND.

A Application of the CG-DG scheme to the Poisson equation

In this short appendix we show the application of the original staggered CG-DG method introduced in [5] to the Poisson equation. Consider the model problem

$$\mathbf{v} = \nabla u, \quad (111)$$

$$\nabla \cdot \mathbf{v} = f(\mathbf{x}). \quad (112)$$

with $\mathbf{v} \cdot \mathbf{n} = 0$ on $\partial\Omega$ and which is nothing else than a first order reformulation of the Poisson equation

$$\nabla^2 u = f(\mathbf{x}), \quad (113)$$

with $\nabla u \cdot \mathbf{n} = 0$ on $\partial\Omega$. Since (111) is a simple definition, according to the choice made in [5], according to which variables that are simple consequences of definitions are defined in the DG space, we choose $\mathbf{v}_h \in \mathcal{U}_h^N$. Since the Laplace equation (113) can be obtained from a variational principle, following [5] we choose $\tilde{u}_h \in \mathcal{W}_h^{N+1}$. With the boundary condition $\mathbf{v} \cdot \mathbf{n} = 0$ on $\partial\Omega$, the weak formulation of the mixed problem above leads to

$$\int_{\Omega} \phi_i \mathbf{v}_h d\mathbf{x} = \int_{\Omega} \phi_i \nabla \tilde{u}_h d\mathbf{x}, \quad (114)$$

$$- \int_{\Omega} \nabla \psi_j \cdot \mathbf{v}_h d\mathbf{x} = \int_{\Omega} \psi_j f(\mathbf{x}) d\mathbf{x}. \quad (115)$$

But since $\mathbf{v}_h \in \mathcal{U}_h^N$ and $\tilde{u}_h \in \mathcal{W}_h^{N+1}$ the first identity (114) holds even strongly, i.e. $\mathbf{v}_h = \nabla \tilde{u}_h$. Inserting in (115) leads to

$$- \int_{\Omega} \nabla \psi_j \cdot \nabla \tilde{u}_h d\mathbf{x} = \int_{\Omega} \psi_j f(\mathbf{x}) d\mathbf{x}, \quad (116)$$

which is simply the *classical* continuous finite element discretization of the Laplace equation [104]. Note that the ansatz spaces of the mixed CG-DG method are chosen differently w.r.t. the Brezzi-Douglas-Marini (BDM) elements [25].

Data Availability

The data can be obtained from the authors on reasonable request.

Conflict of interest

The authors declare that they have no conflict of interest.

References

1. R. Abgrall. Essentially non-oscillatory residual distribution schemes for hyperbolic problems. *J. Comput. Phys.*, 214(2):773–808, 2006.
2. R. Abgrall. A combination of residual distribution and the active flux formulations or a new class of schemes that can combine several writings of the same hyperbolic problem: application to the 1d Euler equations. *Commun. Appl. Math. Comput.*, 5(1):370–402, 2023.
3. R. Abgrall, W. Boscheri, and Y. Liu. Virtual finite element and hyperbolic problems: the PAMPA algorithm. *J. Comput. Phys.*, 546:26, 2026. Id/No 114521.
4. R. Abgrall, S. Busto, and M. Dumbser. A simple and general framework for the construction of thermodynamically compatible schemes for computational fluid and solid mechanics. *Appl. Math. Comput.*, 440:127629, 2023.

5. R. Abgrall, M. Dumbser, and P.-H. Maire. A simple and general framework for the construction of exactly div-curl-grad compatible discontinuous galerkin finite element schemes on unstructured simplex meshes. *J. Comput. Phys.*, 541:114340, 2025.
6. R. Abgrall, J. Lin, and Y. Liu. Active flux for triangular meshes for compressible flows problems. *Beijing J. of Pure and Appl. Math.*, 2:1–33, 2025.
7. R. Abgrall and Y. Liu. Robust pampa scheme in the dg formulation on unstructured triangular meshes: bound preservation, oscillation elimination, and boundary conditions, 2025.
8. R. Abgrall, P.-H. Maire, and M. Ricchiuto. Embedding general conservation-constraints in discretizations of hyperbolic systems on arbitrary meshes: A multidimensional framework. *Mathematical Models and Methods in Applied Sciences*, 36:243–339, 2026.
9. Y. Allaneau and A. Jameson. Connections between the filtered discontinuous galerkin method and the flux reconstruction approach to high order discretizations. *Comput. Methods Appl. Mech. Eng.*, 200:3628–3636, 2011.
10. A. Alonso Rodríguez and A. Valli. Finite element potentials. *Applied Numerical Mathematics*, 95:2–14, 2015.
11. D.N. Arnold, R.S. Falk, and R. Winther. Finite element exterior calculus, homological techniques, and applications. *Acta Numerica*, 15:1–155, 2006.
12. D. Balsara, R. Käppeli, W. Boscheri, and M. Dumbser. Curl constraint-preserving reconstruction and the guidance it gives for mimetic scheme design. *Communications in Applied Mathematics and Computational Science*, 5:235–294, 2023.
13. D.S. Balsara. Multidimensional Riemann problem with self-similar internal structure Part I Application to hyperbolic conservation laws on structured meshes. *J. Comput. Phys.*, 277:163–200, 2014.
14. D.S. Balsara and M. Dumbser. Multidimensional Riemann problem with self-similar internal structure Part II Application to hyperbolic conservation laws on unstructured meshes. *J. Comput. Phys.*, 287:269–292, 2015.
15. D.S. Balsara, S. Garain, A. Taflove, and G. Montecinos. Computational electrodynamics in material media with constraint-preservation, multidimensional Riemann solvers and sub-cell resolution – Part II, higher order FDTD schemes. *Journal of Computational Physics*, 354:613–645, 2018.
16. D.S. Balsara and R. Käppeli. von Neumann stability analysis of globally constraint-preserving DGTD and PNPM schemes for the Maxwell equations using multidimensional Riemann solvers. *Journal of Computational Physics*, 376:1108–1137, 2019.
17. W. Barsukow, R. Loubère, and P.-H. Maire. A node-conservative vorticity preserving finite volume method for linear acoustics on unstructured grids. *Mathematics of Computation*, 2024.
18. X. Blanc, P. Hoch, and C. Lasuen. Composite finite volume schemes for the diffusion equation on unstructured meshes. *Computers & Mathematics with Applications*, 156:207–217, 2024.
19. W. Boscheri, M. Dumbser, M. Ioriatti, I. Peshkov, and E. Romenski. A structure-preserving staggered semi-implicit finite volume scheme for continuum mechanics. *J. Comput. Phys.*, 424:109866, 2021.
20. W. Boscheri, M. Dumbser, R. Loubère, and P.-H. Maire. A structure-preserving and thermodynamically compatible cell-centered Lagrangian finite volume scheme for continuum mechanics. *SIAM J. Num. Anal.* to appear.
21. W. Boscheri, M. Dumbser, and P.-H. Maire. A new thermodynamically compatible finite volume scheme for Lagrangian gas dynamics. *SIAM Journal on Scientific Computing*, 44:A1723–A1751, 2024.
22. W. Boscheri, R. Loubère, and P.-H. Maire. A 3D cell-centered ADER MOOD finite volume method for solving updated Lagrangian hyperelasticity on unstructured grids. *Journal of Computational Physics*, 449:110779, 2022.
23. W. Boscheri, R. Loubère, and P.-H. Maire. An unconventional divergence preserving finite-volume discretization of lagrangian ideal MHD. *Communications on Applied Mathematics and Computation*, 6:1665–1719, 2024.
24. M. Boujoudar, E. Franck, P. Hoch, C. Lasuen, Y. Le Hénaff, and P. Paragot. A composite finite volume scheme for the Euler equations with source term on unstructured meshes. *ESAIM: Proceedings and Surveys*, 77:123–144, 2024.
25. F. Brezzi, J. Douglas, and L.D. Marini. Two families of mixed finite elements for second order elliptic problems. *Numerische Mathematik*, 47:217–233, 1985.
26. L. Brugnano and F. Iavernaro. *Line integral methods for conservative problems*. Chapman et Hall/CRC, Boca Raton, 2016.

27. L. Brugnano and F. Iavernaro. Line integral solution of differential problems. *Axioms*, 7(2):36, 2018.
28. L. Bruni Bruno and E. Zampa. Unisolvent and minimal physical degrees of freedom for the second family of polynomial differential forms. *ESAIM Math. Model. Numer. Anal.*, 56(6):2239–2253, 2022.
29. S. Busto and M. Dumbser. On thermodynamically compatible discontinuous Galerkin methods for continuum mechanics and turbulent shallow water flows. *J. Sci. Comput.*, 93(2):56, 2022.
30. M. Campos Pinto and E. Sonnendrücker. Gauss-compatible Galerkin schemes for time-dependent Maxwell equations. *Math. Comp.*, 85:2651–2685, 2016.
31. E.J. Caramana, D.E. Burton, M.J. Shashkov, and P.P. Whalen. The construction of compatible hydrodynamics algorithms utilizing conservation of total energy. *J. Comput. Phys.*, 146:227–262, 1998.
32. G. Carré, S. Del Pino, B. Després, and E. Labourasse. A cell-centered Lagrangian hydrodynamics scheme on general unstructured meshes in arbitrary dimension. *J. Comput. Phys.*, 228:5160–5183, 2009.
33. P. Castonguay, P.E. Vincent, and A. Jameson. A new class of high-order energy stable flux reconstruction schemes for triangular elements. *J. Sci. Comput.*, 51:224–256, 2012.
34. S. Chiocchetti and M. Dumbser. An exactly curl-free staggered semi-implicit finite volume scheme for a first order hyperbolic model of viscous two-phase flows with surface tension. *Journal of Scientific Computing*, 94:24, 2023.
35. B. Cockburn, S. Hou, and C. W. Shu. The Runge-Kutta local projection discontinuous Galerkin finite element method for conservation laws IV: the multidimensional case. *Math. Comput.*, 54:545–581, 1990.
36. B. Cockburn and C. W. Shu. The Runge-Kutta local projection P1-Discontinuous Galerkin finite element method for scalar conservation laws. *Mathematical Modelling and Numerical Analysis*, 25:337–361, 1991.
37. B. Cockburn and C. W. Shu. The Runge-Kutta discontinuous Galerkin method for conservation laws V: multidimensional systems. *J. Comput. Phys.*, 141:199–224, 1998.
38. A. Del Grosso, W. Barsukow, R. Loubère, and P.-H. Maire. An all-mach cell-centered multi-dimensional finite volume numerical scheme for the euler equations. *Computers & Fluids*, 306:106951, 2026.
39. A. Del Grosso, M.J. Castro, A. Chan, G. Gallice, R. Loubère, and P.H. Maire. A well-balanced, positive, entropy-stable, and multi-dimensional-aware finite volume scheme for 2d shallow-water equations with unstructured grids. *Journal of Computational Physics*, 503:112829, 2024.
40. V. Delmas, R. Loubère, and P.-H. Maire. A node conservative cell-centered finite volume method for solving multidimensional euler equations over general unstructured grids. *Journal of Computational Physics*, 539:114246, 2025.
41. B. Després and C. Mazeran. Symmetrization of Lagrangian gas dynamic in dimension two and multidimensional solvers. *C.R. Mecanique*, 331:475–480, 2003.
42. B. Després and C. Mazeran. Lagrangian gas dynamics in two-dimensions and Lagrangian systems. *Archive for Rational Mechanics and Analysis*, 178:327–372, 2005.
43. M. Dumbser, D.S. Balsara and R. Abgrall. Multidimensional HLLC Riemann Solver for Unstructured Meshes - With Application to Euler and MHD Flows. *J. Comput. Phys.*, 261:172–208, 2014.
44. M. Dubiner. Spectral methods on triangles and other domains. *J. Sci. Comput.*, 6:345–390, 1991.
45. M. Dumbser, D. Balsara, E.F. Toro, and C.D. Munz. A unified framework for the construction of one-step finite-volume and discontinuous Galerkin schemes. *J. Comput. Phys.*, 227:8209–8253, 2008.
46. M. Dumbser, F. Fambri, E. Gaburro, and A. Reinarz. On GLM curl cleaning for a first order reduction of the CCZ4 formulation of the Einstein field equations. *J. Comput. Phys.*, 404:109088, 2020.
47. M. Dumbser, F. Guercilena, S. Köppel, L. Rezzolla, and O. Zanotti. Conformal and covariant Z4 formulation of the Einstein equations: strongly hyperbolic first-order reduction and solution with discontinuous Galerkin schemes. *Physical Review D*, 97:084053, 2018.
48. M. Dumbser, I. Peshkov, E. Romenski, and O. Zanotti. High order ADER schemes for a unified first order hyperbolic formulation of continuum mechanics: Viscous heat-conducting fluids and elastic solids. *J. Comput. Phys.*, 314:824–862, 2016.
49. M. Dumbser, I. Peshkov, E. Romenski, and O. Zanotti. High order ADER schemes for a unified first order hyperbolic formulation of Newtonian continuum mechanics coupled with electro-dynamics. *J. Comput. Phys.*, 348:298–342, 2017.
50. M. Dumbser, O. Zanotti, E. Gaburro, and I. Peshkov. A well-balanced discontinuous Galerkin method for the first-order Z4 formulation of the Einstein-Euler system. *J. Comput. Phys.*, 504:112875, 2024.

51. M. Dumbser, O. Zanotti, and I. Peshkov. High-order discontinuous Galerkin schemes with subcell finite volume limiter and adaptive mesh refinement for a monolithic first-order BSSNOK formulation of the Einstein–Euler equations. *Physical Review D*, 110(8):084015, 2024.
52. M. Dumbser, O. Zanotti, and G. Puppo. Monolithic first-order BSSNOK formulation of the Einstein–Euler equations and its solution with path-conservative finite difference central WENO schemes. *Physical Review D*, 111(10):104072, 2025.
53. Alexandre Ern and Jean-Luc Guermond. Finite element quasi-interpolation and best approximation. *ESAIM Math. Model. Numer. Anal.*, 51(4):1367–1385, 2017.
54. Alexandre Ern and Jean-Luc Guermond. *Finite Elements I: Approximation and Interpolation*, volume 72 of *Texts in Applied Mathematics*. Springer, Cham, 2021.
55. E. Gaburro, M. Ricchiuto, and M. Dumbser. On general and complete multidimensional riemann solvers for nonlinear systems of hyperbolic conservation laws. *Computers and Fluids*, 2026.
56. G. Gallice, A. Chan, R. Loubère, and P.-H. Maire. Entropy stable and positivity preserving godunov-type schemes for multidimensional hyperbolic systems on unstructured grid. *Journal of Computational Physics*, 468:111493, 2022.
57. E. Godlewski and P.-A. Raviart. *Numerical Approximation of Hyperbolic Systems of Conservation Laws*. Springer Verlag, 1996.
58. D. De Grazia, G. Mengaldo, D. Moxey, P.E. Vincent, and S.J. Sherwin. Connections between the discontinuous galerkin method and high-order flux reconstruction schemes. *Int. J. Numer. Methods Fluids*, 75:860–877, 2014.
59. M.E. Gurtin, E. Fried, and L. Anand. *The Mechanics and Thermodynamics of Continua*. Cambridge University Press, 2009.
60. A. Hazra, P. Chandrashekar, and D.S. Balsara. Globally constraint-preserving FR/DG scheme for Maxwell’s equations at all orders. *Journal of Computational Physics*, 394:298–328, 2019.
61. M. R. Hestenes and E. Stiefel. Methods of conjugate gradients for solving linear systems. *Journal of Research of the National Bureau of Standards*, 49:409–436, 1952.
62. R. Hiptmair. Finite elements in computational electromagnetism. *Acta Numerica*, 11:237–339, 2002.
63. P. Hoch. Nodal extension of Approximate Riemann Solvers and nonlinear high order reconstruction for finite volume method on unstructured polygonal and conical meshes: the homogeneous case. *HAL: <https://hal.science/hal-03585115v2>*, 2022.
64. C. Hu and C.W. Shu. Weighted essentially non-oscillatory schemes on triangular meshes. *J. Comput. Phys.*, 150:97–127, 1999.
65. H.T. Huynh. A flux reconstruction approach to high-order schemes including discontinuous galerkin methods. *18th AIAA Computational Fluid Dynamics Conference*, page 4079, 2007.
66. J.M. Hyman and M. Shashkov. Natural discretizations for the divergence, gradient, and curl on logically rectangular grids. *Comput. Math. Appl.*, 33:81–104, 1997.
67. A. Jameson. A proof of the stability of the spectral difference method for all orders of accuracy. *Journal of Scientific Computing*, 45:348–358, 2010.
68. R. Jeltsch and M. Torrilhon. On curl-preserving finite volume discretizations for shallow water equations. *BIT Numerical Mathematics*, 46:S35–S53, 2006.
69. J. Jung and V. Perrier. A curl preserving finite volume scheme by space velocity enrichment. Application to the low Mach number accuracy problem. *Journal of Computational Physics*, 515:113252, 2024.
70. K. Lipnikov, G. Manzini, and M. Shashkov. Mimetic finite difference method. *J. Comput. Phys.*, 257:1163–1227, 2014.
71. Y. Liu, M. Vinokur, and Z.J. Wang. Spectral difference method for unstructured grids I: basic formulation. *J. Comput. Phys.*, 216:780–801, 2006.
72. R. Loubère, P.-H. Maire, and B. Rebourecet. *Handbook of Numerical Methods for Hyperbolic Problems: Basic and Fundamental Issues*, edited by R. Abgrall and C.-W. Shu, chapter 13 Staggered and collocated Finite Volume scheme for Lagrangian hydrodynamics, pages 319–352. North Holland, 2016.
73. R. Loubère, P.-H. Maire, and B. Rebourecet. *Handbook of Numerical Methods for Hyperbolic Problems: Basic and Fundamental Issues*, edited by R. Abgrall and C.-W. Shu, chapter 13 Staggered and collocated Finite Volume scheme for Lagrangian hydrodynamics, pages 319–352. North Holland, 2016.
74. H. Luo, L. Luo, R. Nourgaliev, V.A. Mousseau, and N. Dinh. A reconstructed discontinuous Galerkin method for the compressible Navier–Stokes equations on arbitrary grids. *J. Comput. Phys.*, 229:6961–6978, 2010.

75. H. Luo, Y. Xia, S. Spiegel, R. Nourgaliev, and Z. Jiang. A reconstructed discontinuous Galerkin method based on a Hierarchical WENO reconstruction for compressible flows on tetrahedral grids. *J. Comput. Phys.*, 236:477–492, 2013.
76. P.-H. Maire. A high-order cell-centered lagrangian scheme for two-dimensional compressible fluid flows on unstructured meshes. *J. Comput. Phys.*, 228:2391–2425, 2009.
77. P.-H. Maire, R. Abgrall, J. Breil, and J. Ovardia. A cell-centered lagrangian scheme for two-dimensional compressible flow problems. *SIAM J. Sci. Comput.*, 29:1781–1824, 2007.
78. P.-H. Maire, I. Bertron, R. Chauvin, and B. Rebouret. Thermodynamic consistency of cell-centered Lagrangian schemes. *Computers and Fluids*, 203:104527, 2020.
79. G. Margolin, M. Shashkov, and P.K. Smolarkiewicz. A discrete operator calculus for finite difference approximations. *Computer Methods in Applied Mechanics and Engineering*, 187:365–383, 2000.
80. P. Monk. *Finite Element Methods for Maxwell's Equations*. Oxford University Press, Oxford, 2003.
81. J. Nédélec. Mixed finite elements in R3. *Numerische Mathematik*, 35:315–341, 1980.
82. J. Nédélec. A new family of mixed finite elements in R3. *Numerische Mathematik*, 50:57–81, 1986.
83. V. Perrier. Discrete de-Rham complex involving a discontinuous finite element space for velocities: the case of periodic straight triangular and Cartesian meshes, 2025.
84. V. Perrier. Development of discontinuous Galerkin methods for hyperbolic systems that preserve a curl or a divergence constraint: The case of linear systems, 2026.
85. I. Peshkov and E. Romenski. A hyperbolic model for viscous Newtonian flows. *Continuum Mech. Thermodyn.*, 28:85–104, 2016.
86. D. A. Di Pietro and J. Droniou. An arbitrary-order discrete de Rham complex on polyhedral meshes: exactness, Poincaré inequalities, and consistency. *Foundations of Computational Mathematics*, 23:85–164, 2023.
87. M. Ricchiuto and R. Abgrall. Explicit Runge-Kutta residual distribution schemes for time dependent problems: second order case. *J. Comput. Phys.*, 229(16):5653–5691, 2010.
88. L. Río-Martín, F. Dhaoui, and M. Dumbser. An exactly curl-free finite-volume/finite-difference scheme for a hyperbolic compressible isentropic two-phase model. *Journal of Scientific Computing*, 102:13, 2025.
89. P. L. Roe. “Optimum” upwind advection on a triangular mesh. Technical Report ICASE 90-75, ICASE, 1990.
90. P. L. Roe and D. Sidilkover. Optimum positive linear schemes for advection in two and three dimensions. *SIAM J. Numer. Anal.*, 29(6):1542–1568, 1992.
91. S.K. Sambasivan, M.J. Shashkov, and D.E. Burton. A finite volume cell-centered Lagrangian hydrodynamics approach for solids in general unstructured grids. *Int. J. Numer. Methods Fluids*, 72:770–810, 2013.
92. M.J. Shashkov. *Conservative Finite-Difference Methods on General Grids*. CRC Press, 1996.
93. D. Sidilkover. Spurious vorticity in Eulerian and Lagrangian methods. *Journal of Computational Physics*, 520:113510, 2025.
94. A.H. Stroud. *Approximate Calculation of Multiple Integrals*. Prentice-Hall Inc., Englewood Cliffs, New Jersey, 1971.
95. E. Tadmor. Entropy stability theory for difference approximations of nonlinear conservation laws and related time dependent problems. *Acta Numerica*, 12:451–512, 2003.
96. E.F. Toro. *Riemann Solvers and Numerical Methods for Fluid Dynamics*. Springer, 2009.
97. E. van der Weide and H. Deconinck. Positive matrix distribution schemes for hyperbolic systems. In *Computational Fluid Dynamics*, pages 747–753, New York, 1996. Wiley.
98. P.E. Vincent, P. Castonguay, and A. Jameson. A new class of high-order energy stable flux reconstruction schemes. *J. Sci. Comput.*, 47:50–72, 2011.
99. X. Wang, C. Cheng, H. Luo, and Q. Zhao. A reconstructed direct discontinuous Galerkin method for simulating the compressible laminar and turbulent flows on hybrid grids. *Computers and Fluids*, 168:216–231, 2018.
100. Z.J. Wang, Y. Liu, G. May, and A. Jameson. Spectral difference method for unstructured grids II: Extension to the Euler equations. *J. Sci. Comput.*, 32:45–71, 2007.
101. K.S. Yee. Numerical solution of initial boundary value problems involving Maxwell equation in isotropic media. *IEEE Trans. Antenna Propagation*, 14:302–307, 1966.
102. E. Zampa, A. Alonso Rodríguez, and F. Rapetti. Using the FES framework to derive new physical degrees of freedom for finite element spaces of differential forms. *Adv. Comput. Math.*, 49(17), 2023.
103. E. Zampa, S. Busto, and M. Dumbser. A divergence-free hybrid finite volume / finite element scheme for the incompressible MHD equations based on compatible finite element spaces. *Applied Numerical Mathematics*, 198:346–374, 2024.

-
104. O.C. Zienkiewicz, R.L. Taylor, and J.Z. Zhu. *The finite element method: its basis and fundamentals*. Butterworth-Heinemann, 2013.